DRAFT VERSION MARCH 24, 2023
Typeset using LaTeX **manuscript** style in AASTeX631

Coronal X-Ray Emission from Nearby, Low-Mass, Exoplanet Host Stars Observed by the MUSCLES and Mega-MUSCLES HST Treasury Survey Projects

ALEXANDER BROWN,[1] P. CHRISTIAN SCHNEIDER,[2] KEVIN FRANCE,[3] CYNTHIA S. FRONING,[4,5] ALLISON A. YOUNGBLOOD,[6] DAVID J. WILSON,[3] R. O. PARKE LOYD,[7] J. SEBASTIAN PINEDA,[3] GIRISH M. DUVVURI,[8,1,3] ADAM F. KOWALSKI,[9,8,3] AND ZACHORY K. BERTA-THOMPSON[8,1]

[1]*Center for Astrophysics and Space Astronomy, University of Colorado, 389 UCB, Boulder, CO 80309, USA*

[2]*Hamburger Sternwarte, Gojenbergsweg 112, D-21039, Hamburg, Germany*

[3]*Laboratory for Atmospheric and Space Physics, University of Colorado, 600 UCB, Boulder, CO 80309, USA*

[4]*McDonald Observatory, University of Texas at Austin, Austin, TX 78712, USA*

[5]*Southwest Research Institute, 6220 Culebra Rd., San Antonio, TX 78238, USA*

[6]*Exoplanets and Stellar Astrophysics Lab, NASA Goddard Space Flight Center, Greenbelt, MD 20771, USA*

[7]*School of Earth and Space Exploration, Arizona State University, Tempe, AZ 85287, USA*

[8]*Department of Astrophysical and Planetary Sciences, University of Colorado, Boulder, CO 80309, USA*

[9]*National Solar Observatory, University of Colorado, 3665 Discovery Drive, Boulder, CO 80303, USA*

(Received 2022 December 19; Accepted 2023 March 9)

Submitted to AJ

ABSTRACT

The high energy X-ray and ultraviolet (UV) radiation fields of exoplanet host stars play a crucial role in controlling the atmospheric conditions and the potential habitability of exoplanets. Major surveys of the X-ray/UV emissions from late-type (K and M spectral type) exoplanet hosts have been conducted by the MUSCLES and Mega-MUSCLES Hubble Space Telescope (HST) Treasury programs. These samples primarily consist of relatively old, "inac-

Corresponding author: Alexander Brown
Alexander.Brown@colorado.edu

tive", low mass stars. In this paper we present results from X-ray observations of the coronal emission from these stars obtained using the Chandra X-ray Observatory, the XMM-Newton Observatory, and the Neil Gehrels Swift Observatory. The stars effectively sample the coronal activity of low-mass stars at a wide range of masses and ages. The vast majority (21 of 23) of the stars are detected and their X-ray luminosities measured. Short-term flaring variability is detected for most of the fully-convective ($M \leq 0.35\ M_{\odot}$) stars but not for the more massive M dwarfs during these observations. Despite this difference, the mean X-ray luminosities for these two sets of M dwarfs are similar with more massive ($0.35\ M_{\odot} \leq M \leq 0.6\ M_{\odot}$) M dwarfs at $\sim 5 \times 10^{26}$ erg s^{-1} compared to $\sim 2 \times 10^{26}$ erg s^{-1} for fully-convective stars older than 1 Gyr. Younger, fully-convective M dwarfs have X-ray luminosities between 3 and 6 $\times\ 10^{27}$ erg s^{-1}. The coronal X-ray spectra have been characterized and provide important information that is vital for the modeling of the stellar EUV spectra.

Keywords: M dwarf stars (982), K dwarf stars (876), Stellar x-ray flares (1637), Planet hosting stars (1242)

1. INTRODUCTION

Low mass K and M dwarfs are the focus of major research efforts to discover and characterize their exoplanet systems. It is easier to discover planets orbiting such low mass stars than for solar-like stars using both radial velocity and transit methods, because the effects of the planets on the stellar signal is far larger. Studies have shown the earth-like or super-earth planets are more common around M dwarfs and large gas-giant planets are rarer than for higher mass stars (Dressing & Charbonneau 2015). M dwarfs have very strong surface magnetic fields (see e.g. Shulyak et al. (2019)). Complex 3-6 kG magnetic fields fill and control the outer atmospheres of all M dwarfs (Afram & Berdyugina 2019), leading to bright X-ray emission from their coronae ($T \geq 10^6$ K) and strong ultraviolet emission lines from their chromospheres ($T \sim 10^4$ K) and transition region regions ($T \sim 10^5$ K), which can significantly influence conditions within planetary systems.

Stellar radiation from each spectral region affects an exoplanet in different ways (Ribas et al. (2005), France et al. (2016)). The optical/IR radiation dominates the radiated energy and controls the planet's lower atmospheric and surface heating. X-ray and EUV radiation at wavelengths shortward of 912 Å play a major role in thermospheric heating and erosion of planetary atmospheres (Güdel 2007). FUV/NUV radiation controls the atmospheric chemistry via molecular formation and photolysis. The FUV radiation is dominated by emission in the 1215.67 Å H I Lyman-α line (France et al. (2013), Youngblood et al. (2016)). The EUV region is a mixture of coronal and transition region emission lines that is not easily observable, because of both the obscuration imposed by the interstellar medium and a current lack of suitable observational capability in this spectral region, and thus must be reconstructed using spectral information from the X-ray and FUV regions (Duvvuri et al. 2021).

While considerable efforts have been devoted previously to studying young active M dwarfs in the X-ray and ultraviolet regions, until recently comparatively little was known about the activity levels of older "inactive" M dwarfs. To remedy this lack the MUSCLES ['"Measurements of the Ultraviolet Spectral Characteristics of Low-mass Exoplanetary systems": PI K. France: Program 13650: 125 HST orbits] (France et al. 2016) and Mega-MUSCLES [PI C. Froning: Program 15071: 157 HST orbits] (Wilson et al. (2021), Froning et al. (2022)) HST Treasury programs[1] have conducted an in-depth study of the UV and X-ray spectral energy distributions (SEDs) of K and M dwarf exoplanet hosts with a wide range of rotation periods and activity levels. A sample totaling 23 stars with spectral types from K1 to M8 have been studied with HST UV observations and supporting X-ray observations from Chandra and XMM-Newton. The rotation rates of the stars range from still fast-rotating (few day period) stars to older stars with $\sim$100 day rotation periods. This is important because it is generally assumed that slower rotation links directly to lower magnetic activity levels. Specific aims of these programs include characterizing the energetic radiation environment in the habitable zone of each star, measuring the flare properties on lower activity stars, and providing robust observational inputs to modeling the atmospheric photochemistry and the production of molecular tracers.

[1] The high level science products of these programs, including panchromatiic SEDs, are archived at https://archive.stsci.edu/prepds/muscles/

The purpose of this paper is to provide a detailed overview of all the X-ray observations obtained by the MUSCLES and Mega-MUSCLES projects and to describe the coronal properties of the full sample. The methods used to characterize the X-ray data rely on standard X-ray modeling fitting techniques. Some earlier X-ray results from these projects have appeared in Loyd et al. (2016), Loyd et al. (2018), and Linsky et al. (2020).

2. THE MUSCLES AND MEGA-MUSCLES SAMPLE OF LOW MASS EXOPLANET HOST STARS

The MUSCLES and Mega-MUSCLES targets were chosen to provide spectral energy distributions (SEDs) for stars that include multiple representative examples over spectral types from early K to late M with a range of ages and activity levels. Many young K-M stars already existed in the archives of UV and X-ray missions, but before these new studies observations of older, low activity K-M dwarfs were notably lacking – it was hard to convince proposal reviews to observe "boring" stars. For maximum return the targets were selected from nearby (almost all at distances less than 15 parsecs) stars that are mostly known exoplanet hosts, and thus of individual significance for those studying and modeling exoplanetary systems.

Our goal is to compare the measured coronal properties of our sample with their fundamental physical properties such as mass, rotational period, and age. While physical properties such as effective temperature, mass, and rotational period can be measured fairly directly from observational data, others, particularly age, are much harder to establish. Even directly determinable parameters can be confused in heterogeneous samples where different methods are used to derive the values. Directly observable properties, such as effective temperature as a proxy for mass and rotational period as a proxy for age, can provide secure parameters for differential comparison amongst our sample. The properties of the stars observed are outlined in Table 1, including spectral types, V magnitudes, distances, effective temperatures, masses, rotation periods, and approximate ages. We have aimed to use self-consistent methods for deriving the physical parameters, and minimize extracting heterogeneous values from multiple literature sources. Spectral types were obtained from a critical examination of published values and are primarily from the PMSU survey (Reid, Hawley, & Gizis (1995), Hawley, Gizis, & Reid (1996)) and the CARMENES (Alonso-Floriano et al. 2015) and MEarth (Newton et al. 2014) target sample papers. The very well determined stellar distances are from the parallax data in the GAIA EDR3 catalog (Gaia Collaboration et al.

2016, 2020). Minimizing the uncertainties on these parameters allows the stars to be placed in ordered sequences (e.g. into a reliable mass sequence) with little ambiguity.

2.1. *Effective Temperatures*

The stellar effective temperatures range from early K stars at ∼5000 K to mid-M stars at ∼3000 K. The M8 V star TRAPPIST-1 is the coolest star in the sample at just above 2600 K. The effective temperatures listed are taken primarily from Houdebine et al. (2019), which provides a uniform temperature scale based on the Cousins $(R\text{-}I)_C$ color index for most (17 of 23) of the stars in our sample. Houdebine et al. (2019) provide a detailed comparison to earlier temperature determinations in the literature. Systematic differences are common between different method of temperature determination and can easily be ∼100-200K. The 1σ uncertainty on individual Houdebine et al. (2019) temperatures is ∼40-50 K. The effective temperatures for three additional stars (HD 97658, HD40307, and GJ676A) were estimated from the Houdebine et al. (2019) calibration using $(R\text{-}I)_C$ photometry from Koen et al. (2010). The temperatures derived for HD 97658 and HD40307 were 5155 K and 4963 K respectively, which are comparable to literature values of 5162±6 K (Kulenthirarajah et al. 2017), 5175 K (Takeda & Honda 2020) and 5192 K (Guo et al. 2020) for HD 97658 and 4956 K (Tuomi et al. 2013) for HD 40307. Schweitzer et al. (2019) used spectral fitting of high resolution optical spectra to derive the physical parameters of their CARMENES sample of M dwarf exoplanet hosts and list effective temperatures for eight stars in our sample that are also included in Houdebine et al. (2019). The mean difference between the Houdebine et al. and Schweitzer at al. values is -25 K, with a standard deviation of 35 K, and shows that there is general consistency between different methods of temperature estimation. Effective temperatures for the three remaining stars in our X-ray sample were taken from the following sources: GJ1132 (Berta-Thompson et al. 2015), LHS2686 (Schweitzer et al. 2019), and TRAPPIST-1 (Gonzales et al. 2019).

For comparison, effective temperatures estimated by Pineda, Youngblood, & France (2021) are also presented. Rather than being derived directly from an observable quantity, these values are the end product of a modeling sequence consisting of mass derived from K-band absolute magnitude, radius from a mass-radius

Table 1. MUSCLES - Mega-MUSCLES Exoplanet Host Star Sample

Star	Spectral Type	V (mag)	Distance (pc)	T_{eff} [Houdebine] (K)	T_{eff} [Pineda] (K)	Mass ($M_\odot$)	P_{rot} (days)	Age [Approx.] (Gyr)	Refs.
(1)	(2)	(3)	(4)	(5)	(6)	(7)	(8)	(9)	(10)
HD 97658	K1 V	7.7	21.563±0.010	5155	···	0.77±0.05	34±2	3.8±2.6	1, 2
ϵ Eri	K2 V	3.7	3.220±0.001	5041	···	0.83±0.01	11.68	$0.4^{+0.4}_{-0.2}$	3, 4
HD 40307	K2.5 V	7.1	12.932±0.003	4963	···	0.77±0.05	31.8±6.7	7.0±4.2	5, 2
HD 85512	K6 V	7.7	11.277±0.002	4451	···	0.62±0.01	45.9±0.4	8.2±3.3	5, 2
GJ676A	M0 V	9.6	15.980±0.008	3838	4014^{+94}_{-90}	0.631±0.017	41.2±3.8	···	5
GJ 649	M1 V	9.7	10.391±0.003	3705	3621^{+41}_{-40}	0.524±0.012	23.8±0.1	$4.5^{+3.0}_{-2.0}$	6, 7
GJ 832	M1.5 V	8.7	4.967±0.001	3590	3539^{+79}_{-74}	0.441±0.011	45.7±9.3	(8.4)	5, 8
GJ 667C	M1.5 V	10.2	7.243±0.002	3570	3443^{+75}_{-71}	0.327±0.008	103.9±0.7	≥ 5	5, 9
GJ 15A	M2 V	8.1	3.562±0.001	3656	3601^{+12}_{-11}	0.393±0.009	30.5	∼3	10, 15
GJ 176	M2 V	10.0	9.485±0.002	3542	3632^{+58}_{-56}	0.485±0.012	38.9	$8.8^{+2.5}_{-2.8}$	11, 7
GJ 436	M3 V	10.6	9.775±0.003	3464	3477^{+46}_{-44}	0.425±0.009	44.6±0.2	$8.9^{+2.3}_{-2.1}$	6, 7
GJ 674	M3 V	9.4	4.553±0.001	3478	3404^{+59}_{-57}	0.353±0.008	33.3	0.20	11, 12
GJ 581	M3 V	10.6	6.301±0.001	3423	3424^{+43}_{-42}	0.307±0.007	132.5±6.3	$6.6^{+2.9}_{-2.5}$	5, 7
GJ 163	M3.5 V	11.8	15.135±0.004	3413	3460^{+76}_{-74}	0.405±0.010	61.0±0.3	1-10	5, 13
GJ 849	M3.5 V	10.4	8.815±0.002	3408	3492^{+70}_{-68}	0.465±0.011	32.2±6.3	$4.9^{+3.0}_{-2.1}$	5, 7
GJ 3843	M3.5 V	13.0	13.373±0.006	3353	3278^{+74}_{-70}	0.232±0.006	91.4	···	16
GJ 876A	M4 V	10.2	4.672±0.001	3304	3201^{+20}_{-19}	0.346±0.007	81.0±0.8	$8.4^{+2.2}_{-2.0}$	6, 7
GJ 729	M4 V	10.4	2.976±0.001	3276	3248^{+68}_{-66}	0.177±0.004	2.848±0.001	$0.7^{+0.5}_{-0.3}$	14, 10, 15
GJ 1132	M4 V	13.5	12.607±0.003	(3270)	3196^{+71}_{-70}	0.194±0.005	129	≥ 5	16, 17
GJ 699	M4 V	9.5	1.828±0.001	3266	3223±17	0.161±0.004	145±15	7-10	18, 19
LHS 2686	M4.5 V	14.6	12.189±0.005	(3157)	3119^{+70}_{-68}	0.157±0.004	28.8	···	10
GJ 1214	M4.5 V	14.7	14.642±0.014	3150	3111^{+69}_{-66}	0.181±0.005	125±5	6-10	20
TRAPPIST-1	M8 V	18.8	12.467±0.011	(2628)	2619^{+71}_{-66}	0.090±0.003	3.295±0.003	7.6±2.2	21, 22

NOTE—Rotational period and Age references: 1 Guo et al. (2020), 2 Bonfanti et al. (2015), 3 Donahue, Saar & Baliunas (1996), 4 Janson et al. (2008), 5 Suárez Mascareño et al. (2015), 6 Díez Alonso et al. (2019), 7 Veyette & Muirhead (2019), 8 Bryden et al. (2009), 9 Anglada-Escudé et al. (2013), 10 Newton et al. (2016), 11 Kiraga & Stepien (2007), 12 Montes et al. (2001), 13 Bonfils et al. (2013), 14 Ibañez Bustos et al. (2020), 15 Allen & Herrera (1998), 16 Newton et al. (2018), 17 Berta-Thompson et al. (2015), 18 Toledo-Padrón et al. (2019), 19 Ribas et al. (2018), 20 Mallonn et al. (2018) 21 Vida et al. (2017), 22 Burgasser & Mamajek (2017)

relation, and bolometric luminosity from the combination of J band magnitude and bolometric correction plus distance from parallax. This modeling framework is applicable in the mass range 0.09 - 0.7 $M_\odot$ and are thus applicable to the M dwarfs in our sample but not the early K dwarfs. These effective temperatures form a self-consistent sequence with the mass estimates discussed below.

2.2. *Masses*

The observed stars sample the mass range 0.09 - 0.83 $M_\odot$, with the greatest concentration covering the early- and mid-M stars between 0.1 and 0.5 $M_\odot$. M dwarf masses can also be estimated directly from an observable quantity using the correlation between K band absolute magnitude and mass, with metallicity playing only a minor role (see e.g. Mann et al. (2019)). In Table 1 the mass estimates derived by Pineda, Youngblood, & France (2021), based on the calibration of Mann et al. (2019), are presented, but masses for the 4 K dwarfs are taken from Van Grootel et al. (2014) [HD 97658], Sousa et al. (2008) [HD 40307], and Bonfanti et al. (2015) [ϵ Eri, HD 85512]. The division between stars with radiative cores and fully convective stars occurs at a mass of 0.35 $M_\odot$ (Chabrier & Baraffe 1997).

2.3. *Rotational Periods*

A wide range of rotational periods are covered by the sample stars – a few fast rotators with periods of a few days, many stars with intermediate periods of 20-60 days, plus several very slowly rotating stars with periods as long as $\sim$150 days. This range in rotation should ensure that all levels of coronal activity are sampled. Stellar rotational periods can be derived from long (multi-year) photometric and spectroscopic time series, even for slowly rotating, inactive M dwarfs. Generally, photometric data provides clearer signals with long-lived dark starspot groups modulating the light curve. Rotational signatures in chromospheric emission line spectra, such as Ca II H&K and H Balmer α, are more difficult to establish. For this reason, we give preference to rotational periods derived from photometry in Table 1. These rotation periods relate to the rotation at the latitudes where the strong magnetic field regions emerge through the stellar photosphere, which is potentially far from the stellar equator. Therefore, it is important not to assume that the measured periods represent the equatorial rotation, given that much remains to be learned about differential rotation on low mass stars.

2.4. *Ages*

Determining stellar ages is a nontrivial problem, particularly for M dwarfs. Commonly, when considering magnetic activity among stellar age samples, many papers settle for merely dividing the stars into "young" and "old" stars with the divide at $\sim$1 Gyr. For our study one goal is to understand how stellar rotation and the consequent magnetic activity change with age, hence it is important to have independently determined ages that are not estimated based on stellar activity indicators (such as Ca II HK or X-ray emission) or on rotational periods themselves. The ages listed are from a heterogeneous set of methods, including Galactic kinematic and elemental evolution studies. Evolutionary tracks provide little scope for age separation except for the very youngest stars. Three stars in the MUSCLES/Mega-MUSCLES sample are definitely younger than 1 Gyr (ϵ Eri, GJ 674, GJ 729). Most of the other stars are solar age or older.

2.5. *GJ 15B*

GJ 15B (M3.5 V) forms a wide binary with GJ 15A and is also detected in the GJ 15A Chandra observation. The GJ 15B X-ray source is located 34 arcseconds NE of A. Although GJ 15B is not a known exoplanet host and, thus, is not included in the MUSCLES/Mega-MUSCLES sample, for completeness the properties of its X-ray emission are included in the results presented later in this paper. It is a slow rotator with a period of 167.6 days (Newton et al. 2016). Pinamonti et al. (2018) discuss the detailed properties of the GJ 15 binary system and provide effective temperature and mass estimates for GJ 15B of 3304$\pm$70 K and 0.15$\pm$0.02 $M_\odot$. The temperature estimate is typical for an M3.5 dwarf but the mass is perhaps a little low based on other stars with this spectral type. Their estimate for the bolometric luminosity is 3.3 $\times$ 10^{30} erg s^{-1}, but with a very large uncertainty of a factor of 16.6. Using the observed K band magnitudes for the two stars (A: K=4.02; B: K=5.95) implies a luminosity ratio of 5.9 and, based on the well determined bolometric luminosity for GJ 15A, leads to an improved bolometric luminosity of 1.44 $\times$ 10^{31} erg s^{-1} for B, which falls within the error range of Pinamonti et al. (2018). This larger bolometric luminosity and a mass of 0.15 $M_\odot$ are very similar to those of the M4 V stars in Table 1 and imply that GJ 15B is a fully convective M4 star.

3. X-RAY OBSERVATIONS

Characterization and modeling of the high energy radiation field surrounding exoplanet host stars cannot be successful using UV spectra alone; therefore, when constructing our HST Treasury program surveys it was clear that dedicated X-ray observations were essential to achieve the science goals of the larger projects. A mixture of new dedicated and archival observations were obtained using the Chandra, XMM-Newton, and Swift X-ray observatories. Details of the X-ray observations of these targets are outlined in Table 2.

3.1. *Chandra Observations*

Thirteen stars were observed by Chandra using the ACIS-S3 detector. Dedicated observations were obtained including two (GJ 581, GJ 1214) by proposal 15200539 (PI Brown), four (GJ667C, GJ 176, GJ 436, GJ 876A) by proposal 16200943 (PI France; MUSCLES), five (GJ 15A, GJ 163, GJ 849, GJ 699, LHS 2686) by proposal 19200772 (PI Froning; Mega-MUSCLES). Archival observations were used for HD 97658 (programs 16200348 PI. Miller and 16208530 PI Wheatley), GJ 463 (program 14200978, PI Ehrenreich), and GJ3843 (=L980-5, program 81200661, PI Wright).

3.2. *XMM-Newton Observations*

Nine stars were observed by XMM using the EPIC detectors. Dedicated observations were obtained including two (HD 40307, HD 85512) by proposal 076381 (PI Brown), two (ϵ Eri, GJ 832) by proposal 074801 (PI France; MUSCLES), four (GJ 649, GJ 674, GJ 729, TRAPPIST-1) by proposal 081021 (PI Froning; Mega-MUSCLES). Additional archival observations were used for GJ 1132 (program 080493, PI King) and TRAPPIST-1 (program 080444, PI Wheatley).

3.3. *SWIFT Observations*

No Chandra or XMM-Newton observations exist for Mega-MUSCLES target GJ 676A, and we have used archival Swift XRT observations to measure the X-ray activity level for this star. The two most useful data sets were obtained on 2018 June 19 (ObsIDs: 0001078003-4; 3157 s exposure) and on 2019 Apr 1/2

Table 2. MUSCLES - Mega-MUSCLES X-ray Observations

Star	Spectral Type	Instrument	Exposure Time (ks)	Observation Date - Start Time [UT]	ObsID
HD 97658	K1 V	ACIS	12.9	2015-10-17 13:37:51	16668
...	...	ACIS	19.2	2015-12-11 12:39:18	18724
...	...	ACIS	19.2	2016-03-05 15:59:55	18725
ϵ Eri	K2 V	EPIC	4.9(pn);10.5(MOS)	2015-02-02 08:16:05	0748010101
HD 40307	K2.5 V	EPIC	12.5(pn);5.0(MOS)	2015-03-17 02:47:53	0763810101
HD 85512	K6 V	EPIC	14.57	2015-05-24 10:09:51	0763810201
GJ676A	M0 V	Swift	6.71	2018-06-19/2019-04-1/2	See Sect. 3.3
GJ 649	M1 V	EPIC	18.0	2018-03-03 13:44:39	0810210401
GJ 832	M1.5 V	EPIC	8.9(pn);11.5(MOS)	2015-10-11 02:50:32	0748010201
GJ 667C	M1.5 V	ACIS	9.1/18.2	2015-08-07 04:43:16/ 14:10:52	17318/17317
GJ 15A	M2 V	ACIS	23.8	2019-02-12 17:25:17	20617
GJ 176	M2 V	ACIS	9.6	2015-02-28 00:13:08	17320
...	...	ACIS	19.6	2015-03-02 03:03:26	17319
GJ 436	M3 V	ACIS	18.8	2013-02-16 14:51:23	14459
...	...	ACIS	18.9	2013-04-18 08:31:13	15537
...	...	ACIS	19.8	2013-06-18 06:55:32	15536
...	...	ACIS	18.8	2014-06-23 10:42:32	15642
...	...	ACIS	9.1	2015-06-25 02:26:52	17322
...	...	ACIS	19.6	2015-06-26 01:22:02	17321
GJ 674	M3 V	EPIC	30.4	2018-04-03 06:14:25	0810210301
GJ 581	M3 V	ACIS	47.6	2014-06-12 08:19:02	15724
GJ 163	M3.5 V	ACIS	28.6	2019-03-04 18:24:00	20621
GJ 849	M3.5 V	ACIS	28.0	2019-06-14 23:15:36	20620
GJ 3843	M3.5 V	ACIS	6.9	2016-12-16 19:10:13	18938
GJ 876A	M4 V	ACIS	9.9	2015-06-04 17:18:25	17316
...	...	ACIS	19.8	2015-06-05 05:15:14	17315
GJ 729	M4 V	EPIC	23.0	2018-04-20 04:59:03	0810210201
GJ 1132	M4 V	EPIC	46.6	2019-01-10 10:06:49	0804930201
GJ 699	M4 V	ACIS	26.7	2019-06-17 08:51:05	20619
LHS 2686	M4.5 V	ACIS	26.7	2019-03-08 11:56:58	20618
GJ 1214	M4.5 V	ACIS	30.5	2014-06-17 03:20:29	15725
TRAPPIST-1	M8 V	EPIC	24.6	2018-12-10 03:52:57	0810210101

(ObsIDs: 0001078006-9; 3554 s exposure). Combined these observations provide a background-corrected total of 32.6 source counts and a source count rate of 4.86±0.85 10^{-3} ct s^{-1} (5.7 σ detection). The individual source count rates for the 2018 and 2019 data were 5.68±1.34 10^{-3} ct s^{-1} (4.2 σ detection) and 4.1±1.1 10^{-3} ct s^{-1} (3.8 σ detection) respectively. There is no evidence for significant source variability, although we note that the number of counts is very limited.

4. X-RAY DATA ANALYSIS

The X-ray data were analyzed with standard analysis techniques for the various X-ray detectors used. Timing and spectral studies were conducted when the number of detected source counts was sufficient. Analysis was typically performed on standard pipeline-processed datasets obtained from the mission archives. The X-ray spectra were fitted using the XSPEC software package (Versions 12.5.1 - 12.12.0 – Arnaud (1996); Dorman, Arnaud, & Gordon (2003)). The spectral parameterization provides estimates of the characteristic coronal temperature and the associated volume emission measure. Depending on the number of source counts collected either one-temperature (1T), two-temperature (2T), or in some cases even three-temperature (3T) parameterizations using VAPEC spectral models (Smith et al. 2001) were possible. All the stars observed are very close (mostly less than 15 pc) to the Sun and thus have very low intervening hydrogen column densities (N_H), which cannot be constrained by CCD-resolution *Chandra* and *XMM-Newton* spectra. Therefore, we adopted a fixed value of N_H, typically 1×10^{19} cm^{-2}, when fitting the spectra, rather than attempting to derive N_H directly from the X-ray data.

The results from analysis of our X-ray observations are presented in Tables 3 and 4 for the XMM-Newton observations and Tables 5 and 6 for the Chandra observations. These tables provide information on the detected source counts and the background-corrected count rate, presence or absence of significant source variability, the observed 0.3-10 keV flux, the X-ray luminosity and X-ray to bolometric luminosity ratio in the same energy range, and the derived coronal temperature (kT_1) and volume emission measure (VEM_1) for the dominant thermal component, the temperature (kT_2) and volume emission measure (VEM_2) for any identifiable secondary thermal component, and the reduced χ^2 for the fitting parameterization. For variability, a question mark indicates uncertainty, while parentheses indicate long-term variability.

4.1. *Chandra Observations*

The ACIS data were analyzed using standard CIAO (Fruscione et al. 2006) software tools on the standard pipeline-processed dataset obtained from the mission archive. Source events from the ACIS observations were extracted using extraction circles with radii of 5 CCD pixels (2.5 arcseconds).

A barycentric correction was applied to the times in each event list using the CIAO tool *axbary*. Each dataset was tested for source variability using the CIAO tool *glvary*. This tool searches for variability using the Gregory-Loredo algorithm, which tests for nonrandom bunching of the event times across multiple time bins. *glvary* is the standard tool used to test for variability in the major Chandra source catalogs. *glvary* produces a variability index (VARINDEX) which ranges from 0 to 10, with values of 5 or above indicating a variable source.

4.2. *XMM-Newton Observations*

XMM-Newton observations were obtained using primarily the EPIC pn and MOS detectors. Background particle radiation can seriously degrade the EPIC data and high background time intervals were removed from the data before spectral analysis but not for light curve construction. Source extraction circle sizes are usually around 15 arcsec, sometimes slightly adjusted for very weak or strong sources. The background was estimated from detector regions on the same detector chip, which are much larger than the source size. The spectra from the pn and the two MOS detectors were jointly analyzed with XSPEC. Because flare signatures are usually well visible in the light curves, no formal variability analysis has been performed.

4.3. *Swift Observations*

Too few counts were detected for GJ 676A by Swift for any detailed spectral fitting. Therefore, we assume a coronal temperature of 0.24 keV (2.8 MK), typical for most of the other quiescent early-mid M dwarfs in our sample, sub-solar abundances (0.4 solar) and a interstellar hydrogen column of 10^{19} cm^{-2} as inputs for estimating its X-ray flux and luminosity. The X-ray flux was estimated using WebPIMMS[2] and APEC spectral models (Smith et al. 2001) . The assumed abundance has only a small influence on

[2] The Portable Interactive Multi-Mission Simulator, https://heasarc.gsfc.nasa.gov/cgi-bin/Tools/w3pimms/w3pimms.pl

Table 3. MUSCLES K1-M0 Dwarf Datasets and Measured Coronal X-ray Properties

	ϵ Eri	HD 40307	HD 85512	HD 97658	GJ 676A
Instrument	EPIC[a]	EPIC[a]	EPIC[a]	ACIS	SWIFT-XRT
Source Counts (ct)	3.8×10^4	71	283	43	32
Count Rate (ct s^{-1})	6.05 ± 0.03	$(4.2 \pm 0.7) \times 10^{-3}$	$(16.6 \pm 1.4) \times 10^{-3}$	$(8.3 \pm 1.4) \times 10^{-4}$	$(4.9 \pm 0.9) \times 10^{-3}$
Variable (Yes/No)	(Y)[b]	N	N	N?	N
f_X (erg cm^{-2} s^{-1})	$(9.2\pm0.1)\times10^{-12}$	$(7\pm2)\times10^{-15}$	$(1.9^{+0.4}_{-0.3})\times10^{-14}$	$(7.7\pm1.3)\times10^{-15}$	$(9.7\pm1.7)\times10^{-14}$
$\log L_X$ (erg s^{-1})	28.06 ± 0.06	26.15 ± 0.15	26.46 ± 0.09	26.63 ± 0.08	27.47 ± 0.08
$\log L_X/L_{bol}$	-5.03 ± 0.06	-6.80 ± 0.13	-6.26 ± 0.09	-6.59 ± 0.08	-5.06 ± 0.08
N_H (10^{20} cm^{-2})	$0.5^{+1.1}_{-0.5}$	0.1[c]	0.1[c]	0.1[c]	0.1[c]
kT_1 (keV)	$0.12^{+0.09}_{-0.02}$	0.15 ± 0.06	$0.25^{+0.04}_{-0.03}$	0.23 ± 0.04	···
VEM_1 (10^{49} cm^3)	53^{+45}_{-19}	$1.2^{+3.0}_{-0.6}$	2.3 ± 0.3	2.0 ± 1.3	···
kT_2 (keV)	0.32 ± 0.01	···	···	···	···
VEM_2 (10^{49} cm^3)	78.4^{+11}_{-10}	···	···	···	···
kT_3 (keV)	$0.70^{+0.04}_{-0.07}$	···	···	···	···
VEM_3 (10^{49} cm^3)	$22.2^{+5.1}_{-3.5}$	···	···	···	···
Red. χ^2	1.28[d]	1.00	0.95[e]	1.95	···

[a] For XMM-Newton summed EPIC (pn+mos1+mos2) – Fit performed using C-statistic, χ^2 provided for reference only.

[b] No significant variability during the MUSCLES EPIC-pn observation but long-term variability present (see Sect. 6.1).

[c] Fixed $N_H = 1 \times 10^{19}$ cm^{-2} for the fit.

[d] Adjusted abundances: Low-FIP (Fe, Mg): $0.47^{+0.08}_{-0.06}$, Mid-FIP (C, N, O, Si, S): $0.39^{+0.09}_{-0.11}$, High-FIP (Ne, Ar): $0.46^{+0.09}_{-0.13}$

[e] Iron abundance fixed to 0.05; upper limit 0.16.

the estimated flux with abundances of 0.2 solar and 1.0 solar producing a 4% flux decrease and a 4% flux increase respectively. The assumed temperature has a larger effect. Increasing the temperature has less effect than lowering it. Doubling the temperature to 0.48 keV (5.6 MK) increases the flux by only 5%, but decreasing the temperature to 0.15 keV (1.8 MK) leads to a flux estimate 19% smaller.

Table 4. XMM-Newton M Dwarf Datasets and Measured Coronal X-ray Properties [a] [b] [c]

	GJ 832	GJ 649	GJ 674	GJ 729	GJ 1132	TRAPPIST-1
Source Counts (ct)	224	970	22,484	7,015	104	107
Count Rate (ct ks^{-1})	25±2	54±3	740±6	305±14	2.2±0.4	5.4±0.6
Variable (Yes/No)	N	N	Y	Y	Y?	(Y)
f_X (10^{-14} ergs cm^{-2} s^{-1})	4.0±0.5	$12.5^{+3.2}_{-1.5}$	134±2	568±7	$1.12^{+0.33}_{-0.27}$	$1.15^{+0.23}_{-0.22}$
$\log L_X$ (erg s^{-1})	26.07 ± 0.06	27.21 ± 0.06	27.52 ± 0.06	27.78 ± 0.06	26.33 ± 0.06	26.33 ± 0.06
$\log L_X/L_{bol}$	-5.95±0.06	-5.02±0.06	-4.26±0.06	-3.41±0.06	-4.89±0.06	-4.04±0.06
kT_1 (keV)	0.23±0.02	$0.12^{+0.04}_{-0.01}$	$0.12^{+0.01}_{-0.02}$	0.15±0.02	(0.086)	(0.2)
VEM_1 (10^{49} cm^3)	0.18±0.02	$0.83^{+0.05}_{-0.03}$	$1.28^{+0.18}_{-0.23}$	1.83 ± 0.02	$0.38^{+0.15}_{-0.13}$	1.06±0.47
kT_2 (keV)	···	$0.62^{+0.07}_{-0.06}$	$0.27^{+0.01}_{-0.02}$	0.34±0.02	(0.86)	(0.8)
VEM_2 (10^{49} cm^3)	···	$0.31^{+0.01}_{-0.03}$	$1.84^{+0.14}_{-0.18}$	3.32 ± 0.04	0.03 ± 0.01	0.82 ± 0.32
kT_3 (keV)	···	···	$0.81^{+0.05}_{-0.03}$	$0.75^{+0.04}_{-0.03}$	···	···
VEM_3 (10^{49} cm^3)	···	···	$0.65^{+0.07}_{-0.09}$	2.71 ± 0.03	···	···
Red. χ^2	1.15[d]	1.32[d]	1.14[d]	1.18[e]	1.29[f]	1.29[f]

[a] EPIC pn only

[b] Fit performed using C-statistic, χ^2 provided for reference only.

[c] Fixed $N_H = 1 \times 10^{19}$ cm^{-2} for the fit.

[d] Abundances fixed to 0.4 solar

[e] Adjusted abundances: Low-FIP (Fe, Mg): $0.47^{+0.08}_{-0.06}$, Mid-FIP (C, N, O, Si, S): $0.39^{+0.09}_{-0.11}$, High-FIP (Ne, Ar): $0.46^{+0.09}_{-0.13}$

[f] Temperatures fixed. Abundances fixed to 0.4 solar.

Table 5. MUSCLES Chandra/ACIS M Dwarf Datasets and Measured Coronal X-ray Properties

	GJ 176	GJ 436	GJ 581	GJ 581(flare)	GJ 667C	GJ 876(low)	GJ 876(high)	GJ 1214
Source Counts (ct)	225	281	102	250	168	121	910	···
Count Rate (ct ks^{-1})	7.7±0.5	2.5±0.2	2.5±0.3	35.7±2.3	6.0±0.5	12.1±1.1	45.9±1.5	≤0.14 (90% Conf.)
Variable (Yes/No)	N	N	Y	Y	N	Y	Y	(Y)
f_X (10^{-14} erg cm^{-2} s^{-1})	4.8±0.3	1.2±0.1	1.8±0.2	21.5±1.4	3.9±0.3	9.1±0.8	30.5±1.0	≤0.11[d]
log L_X (erg s^{-1})	26.71±0.03	26.14±0.04	25.93±0.05	27.01±0.06	26.39±0.03	26.38±0.06	26.90±0.05	≤25.45
log L_X/L_{bol}	-5.42±0.04	-5.84±0.04	-5.73±0.05	-4.65±0.06	-5.35±0.04	-5.32±0.06	-4.80±0.06	≤-5.7
kT_1 (keV)	0.31±0.02	0.39±0.03	0.26±0.02	0.99±0.08	0.41±0.03	0.80±0.14	0.68±0.04	···
VEM_1 (10^{49} cm^3)	5.3±1.5	1.04±0.25	1.00±0.30	2.64±0.66	1.81±0.54	0.37±0.15	6.5±1.2	···
kT_2 (keV)	···	···	···	0.27±0.06	···	0.14±0.04	0.24±0.08	···
VEM_2 (10^{49} cm^3)	···	···	···	2.30±0.97	···	1.3±1.6	1.8±1.2	···
Red. χ^2	0.88[a]	0.7[b]	1.13[c]	1.23[d]	1.63[e]	0.98[d]	1.03[f]	···

[a] Adjusted abundances: Fe=0.41±0.18

[b] Adjusted abundances: Fe=0.17±0.11

[c] Adopted sub-solar abundances: Fe=0.15

[d] Adopted solar abundances: Fe=1.0

[e] Adjusted abundances: Fe=0.19±0.12

[f] Adopted sub-solar abundances: Fe=0.195; measured Fe=0.17±0.04

Table 6. Mega-MUSCLES M Dwarf Datasets and Measured Coronal X-ray Properties

	GJ 15A	GJ 15B	GJ 163	GJ 849	GJ 3843	GJ 699 (all)	GJ 699 (quiet)	LHS2686
Instrument	ACIS-S3	ACIS-S3	ACIS-S3	ACIS-S3	ACIS-S3	ACIS-S3	ACIS-S3	ACIS-S3
Source Counts (ct)	175	100	41	77	···	137	94	469
Count Rate (ct ks^{-1})	7.3±0.6	4.2±0.4	1.4±0.3	2.8±0.3	≤0.86	5.2±0.5	4.0±0.4	17.6 ± 0.8
Variable (Yes/No)	N	Y	N	N	···	Y	N	Y
f_X (10^{-14} erg cm^{-2} s^{-1})	8.5±0.7	5.1±0.5	1.97±0.34	4.74±0.57	≤0.81‘[a]	6.30±0.55	4.83±0.52	15.3±0.7
log L_X (erg s^{-1})	26.11±0.04	25.89±0.08	26.73±0.06	26.64±0.06	≤25.28	25.40±0.06	25.29±0.06	27.44±0.06
log L_X/L_{bol}	-5.82±0.04	-5.27±0.08	-5.19±0.08	-5.40±0.06	≤-5.15	-5.71±0.06	-5.83±0.06	-3.60±0.06
kT_1 (keV)	0.45±0.07	0.56±0.12	0.51±0.22	0.32±0.05	···	0.54±0.11	0.49±0.12	0.90±0.05
VEM_1 (10^{49} cm^3)	1.22±0.33	0.68±0.18	4.9±3.8	4.4±1.9	···	0.23±0.07	0.11±0.08	12.1±3.0
Red. χ^2	1.12[b]	1.25[c]	0.87[b]	1.35[b]	···	1.03[d]	1.20[e]	1.02[f]

[a] Adopted kT=0.43 keV and solar abundances: Fe=1.0

[b] Adopted sub-solar abundances: Fe=0.195

[c] Adopted sub-solar abundances: Fe=0.195,Using L_{bol} = 1.44 × 10^{31} erg s^{-1}

[d] Adjusted abundances: Fe=0.19±0.12; Adopted N_H = 5 × 10^{18} cm^{-2}

[e] Adjusted abundances: Fe=0.36±0.23; Adopted N_H = 5 × 10^{18} cm^{-2}

[f] Adjusteded sub-solar abundances: Fe=0.61±0.12

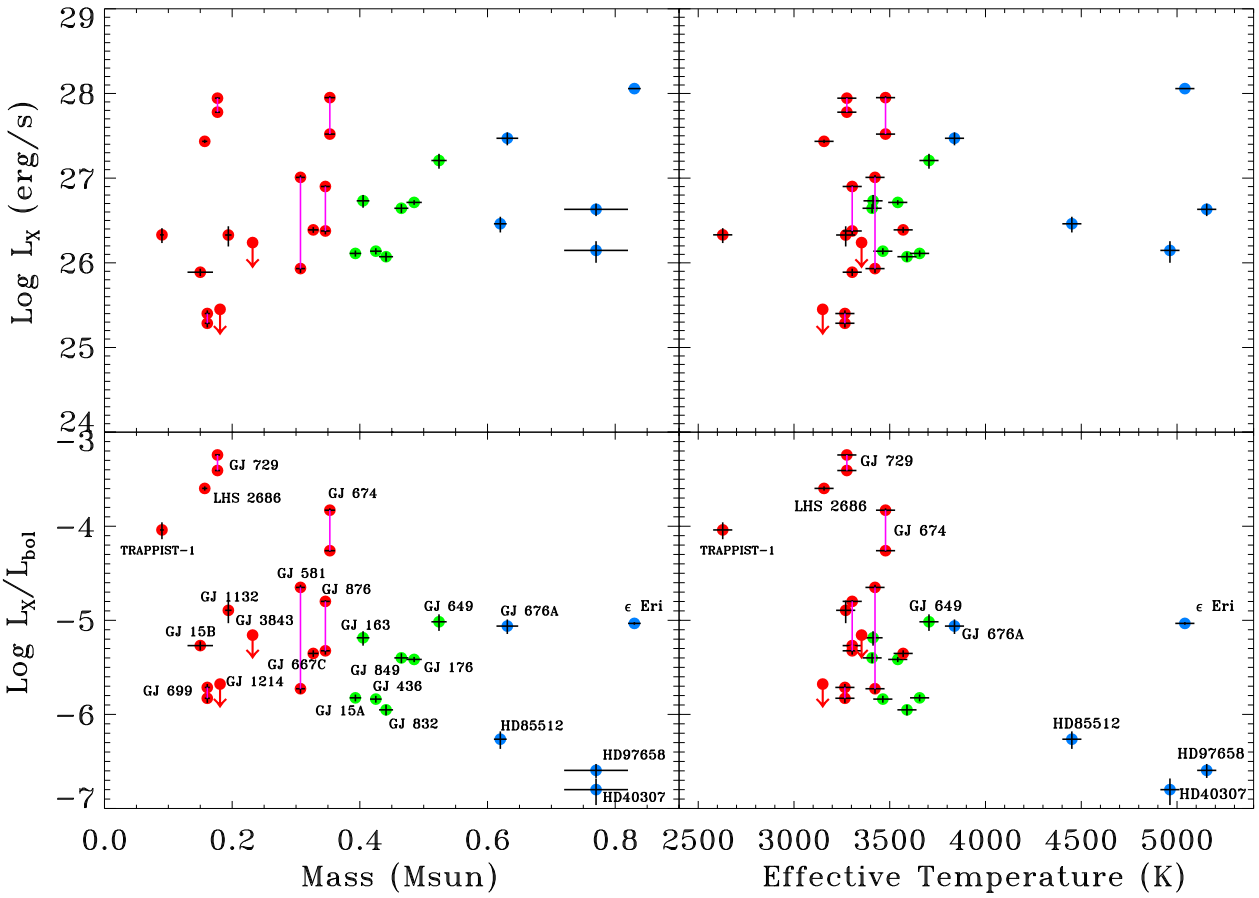

Figure 1. X-ray (0.3 - 10.0 keV) luminosity and X-ray-to-bolometric luminosity ratio as a function of stellar mass and effective temperature. Observations of the same star in quiescent and flaring states are connected by vertical lines. Color coding: blue - M$\geq$ 0.6 $M_\odot$; green - 0.35$\leq$ M $\leq$ 0.6 $M_\odot$; red M $\leq$ 0.35 $M_\odot$. Error bars are plotted in black with some being smaller than the plotting symbols.

5. CORONAL PHYSICAL PROPERTIES

The derived X-ray luminosities and the X-ray-to-bolometric luminosity ratios are the primary observables that can be compared to the stellar physical properties discussed in Sect. 2.

Figures 1 and 2 show the distributions of the soft-X-ray luminosity and X-ray-to-bolometric luminosity ratio with stellar mass, effective temperature, rotational period and age, respectively. Where feasible, identification of the individual stars in the sample is provided, because many exoplanet researchers will be interested about particular stars and how they fall within the overall sample.

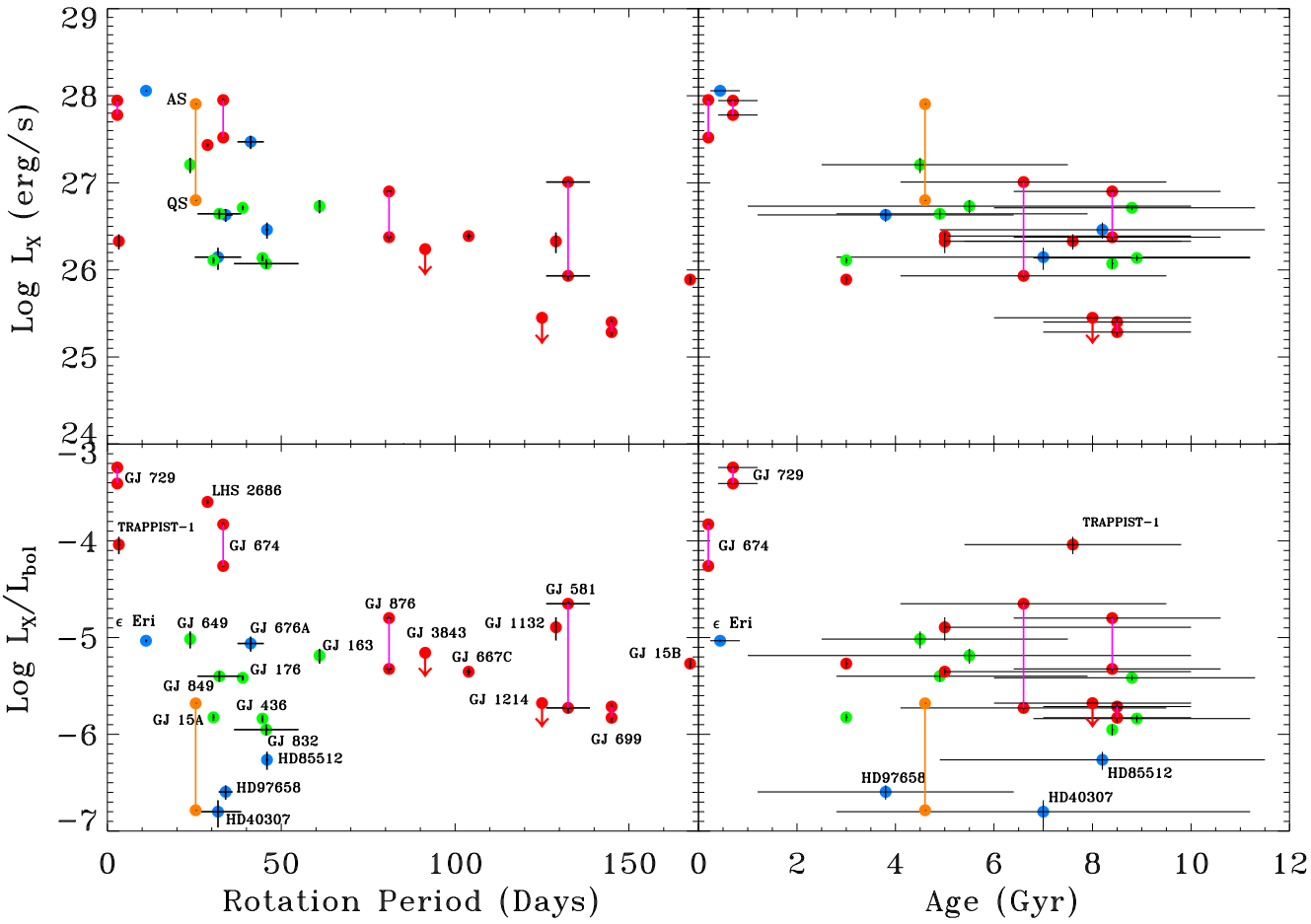

Figure 2. X-ray luminosity and X-ray-to-bolometric luminosity ratio as a function of stellar rotation period (left panels) and age (right panels). For comparison, the equivalent numbers for the Quiet Sun (QS) and Active Sun (AS) are shown as orange symbols. Most stars in the sample are older than the Sun (4.5 Gyr). Three stars are younger than 1 Gyr. For older stars the age uncertainties are large. Color coding as in Fig. 1.

Generally the X-ray luminosities of the sample lie between 10^{26} and 10^{28} erg s^{-1}, with only GJ 699 being detected at a significantly lower luminosity aided by its proximity at a distance of only 1.8 pc . The mean X-ray luminosities for the more massive (0.35 $M_\odot \leq M \leq 0.6\ M_\odot$) M dwarfs is $\sim 5 \times 10^{26}$ erg s^{-1} compared to $\sim 2 \times 10^{26}$ erg s^{-1} for fully-convective stars older than 1 Gyr. Younger, fully-convective M dwarfs have X-ray luminosities between 3 and 6×10^{27} erg s^{-1}. For comparison, the corresponding X-ray luminosities from the Quiet and Active Sun are 6.31×10^{26} and 8.04×10^{27} erg s^{-1} respectively and the L_X/L_{bol} ratios are 1.64×10^{-7} and 2.09×10^{-6} (Linsky et al. 2020). This sensitivity level is imposed by the capabilities

of existing X-ray observatories, but, nevertheless the vast majority of the sample provided secure X-ray detections and multiple examples of significant coronal variability. When considered in terms of X-ray to bolometric luminosity, the major increase in bolometric luminosity from late-M to early-K stars contributes to the trend where X-ray emission from non-saturated coronae becomes a larger component of the stellar emission for stars of lower mass (Fleming et al. 1995).

6. CORONAL VARIABILITY

The X-ray emission from K and M dwarfs typically shows considerable variability that results in major changes of the radiation field impacting exoplanets. This variability is not confined to the most active, rapidly-rotating stars but extends to the oldest, least active stars as well. We have examined all our data sets for short-term variability and compared our results with those published by others for long-term variability. For discussion we divide our sample into three mass ranges.

During the MUSCLES/Mega-MUSCLES X-ray observations flare outbursts are seen from seven of ten fully-convective stars. Younger fully-convective stars all showed multiple flare outbursts. However, in all cases only a small portion of the time sampled contained flares. For example, even for GJ 876A (see Fig. 4) the X-ray flux is only above three times the quiescent level for 31% of the observation. For seven fully-convective stars stars older than 1 Gyr six flare outbursts are seen over 226 ks. In contrast, the three older K dwarfs show zero discernible flares over 78 ks and seven more massive M dwarfs show zero discernible flares over 244 ks.

6.1. *K - M0 Dwarfs – M≥0.6 $M_\odot$*

Our sample contains 5 stars in this mass range with only ϵ Eri considered to be young. None of the stars shows X-ray flaring in dedicated MUSCLES X-ray observations but archival observations show the presence of some long-term variability.

ϵ Eri (HD 22409, GJ 144; K2 V) : This star is the youngest K dwarf in our sample and shows bright X-ray emission with a luminosity exceeding 10^{28} erg s^{-1}. The MUSCLES XMM-Newton EPIC pn observation of ϵ Eri does not show significant coronal variability. Loyd et al. (2018) observed an FUV flare with HST immediately preceding the EPIC pn observations and an X-ray flare decay was possibly seen by the EPIC

MOS detectors but with large error bars. Two small FUV enhancements during the EPIC pn observation produced no detectable corresponding X-ray response. More extensive monitoring of its X-ray emission with a further 7 observations over the following 3.5 years shows quiescent flux levels up to twice that seen in 2015 and additional short-term flaring to over 2.1 $\times$ 10^{-11} erg cm^{-2} s^{-1} (Coffaro et al. 2020). These variations are reasonably consistent with a likely 2.9 year period activity cycle seen in Ca II HK detected by Metcalfe et al. (2013).

The data for HD 40307 (GJ 2406; K2.5 V), HD 85512 (GJ 370, K6 V), and HD 97658 (K1 V), and GJ 676A (M0 V) show no statistically significant variability, However, for HD 97658 there is a suggestion of variability between the 2015-10-17 Chandra observation (count rate 1.31$\pm$0.35$\times$10^{-3} ct s^{-1}; 3.7σ), which showed twice the count rate seen in the two later observations (2015-12-11: count rate 0.73$\pm$0.22$\times$10^{-3} ct s^{-1}; 3.3σ, and 2016-03-05: count rate 0.61$\pm$0.21$\times$10^{-3} ct s^{-1}; 2.9σ).

6.2. *Early-Mid M Dwarfs (M1-3.5) with M$\geq$0.35 M$_\odot$*

Seven early-mid M dwarf stars fall into this mass category and none of them show significant X-ray flaring. While GJ 667C (HD156384C) is usually quoted to have an M1.5 V spectral type, its mass (0.327 M$_\odot$) and effective temperature (3443 K) indicate that it is more likely to be a fully convective star. Therefore, GJ 667C is discussed in Sect. 6.3

GJ 15A (M2 V) and GJ 15B (M4 V) : The two stars in this wide binary were observed in the same ACIS-S3 observations and show independent patterns of variability (see Fig. 3). Both stars are close to the boundary of significant variability with GJ 15B above the threshold (glvary VARINDEX = 8) and GJ 15A below (glvary VARINDEX = 1).

GJ 649 (M1 V), GJ 832 (HD 204961; M1.5 V), GJ 176 (HD 285968, M2 V, Fig. 12), GJ 436 (M3 V, Fig. 13), GJ 163 (M3.5 V), GJ 849 (M3.5 V, Fig. 15): All showed no statistically significant variability and the light curves for some of these stars are shown at the end of this paper in Appendix A. The absence of detectable X-ray flaring on these stars is somewhat surprising because FUV flares were clearly seen in simultaneous HST observations of GJ 176 (see Fig. 14). Low count rates for many of these stars necessitate light curves with large temporal bins that may smooth out small scale flare signals.

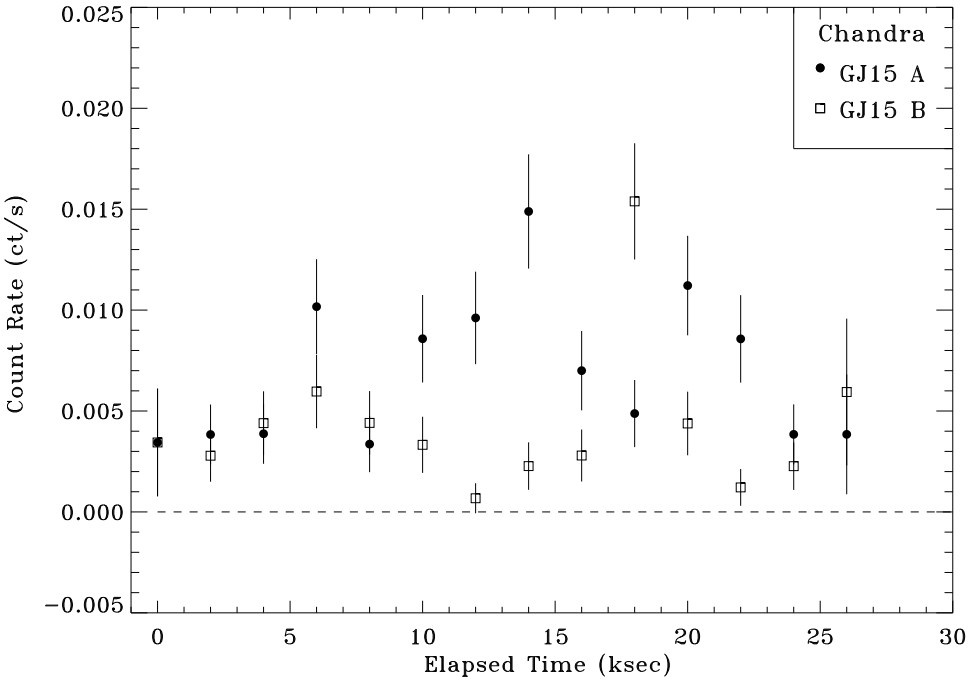

Figure 3. Chandra ACIS-S3 lightcurve of GJ 15 A and B using 2 kilosecond sampling bins. 1σ error bars are plotted.

6.3. *Fully Convective M Dwarfs (M3-8) with M≤0.35 $M_\odot$*

There are ten fully convective stars in the sample and all but one of those that are detected (plus GJ 15B) show short-term variability.

GJ 876A (M4 V) : This star is a fairly slowly rotating mid-M dwarf but shows significant FUV and X-ray flaring activity (France et al. (2012), France et al. (2016)). Rivera et al. (2005) measured an initial photometric rotation period of 96.7 days and Díez Alonso et al. (2019) more recently produced a revised period of 81.0 days. This rotational period indicates that the rotation is still slowing and significant rotational evolution is yet to occur. The Chandra X-ray light curve is shown in Fig. 4. Dramatic soft X-ray flaring is present throughout the observations. The data were obtained in two segments with an initial "low" state observation and then a longer "high" state observation containing multiple flares that occur throughout the 20 ks observation. The minimum 0.3-10.0 keV luminosity at the start of the first segment was 1.1×10^{26} erg s^{-1}, compared to a maximum flare peak luminosity of 2.6×10^{27} erg s^{-1}, which is an increase by a factor of 23. The total energies over the same energy range in the initial large and smaller final flares

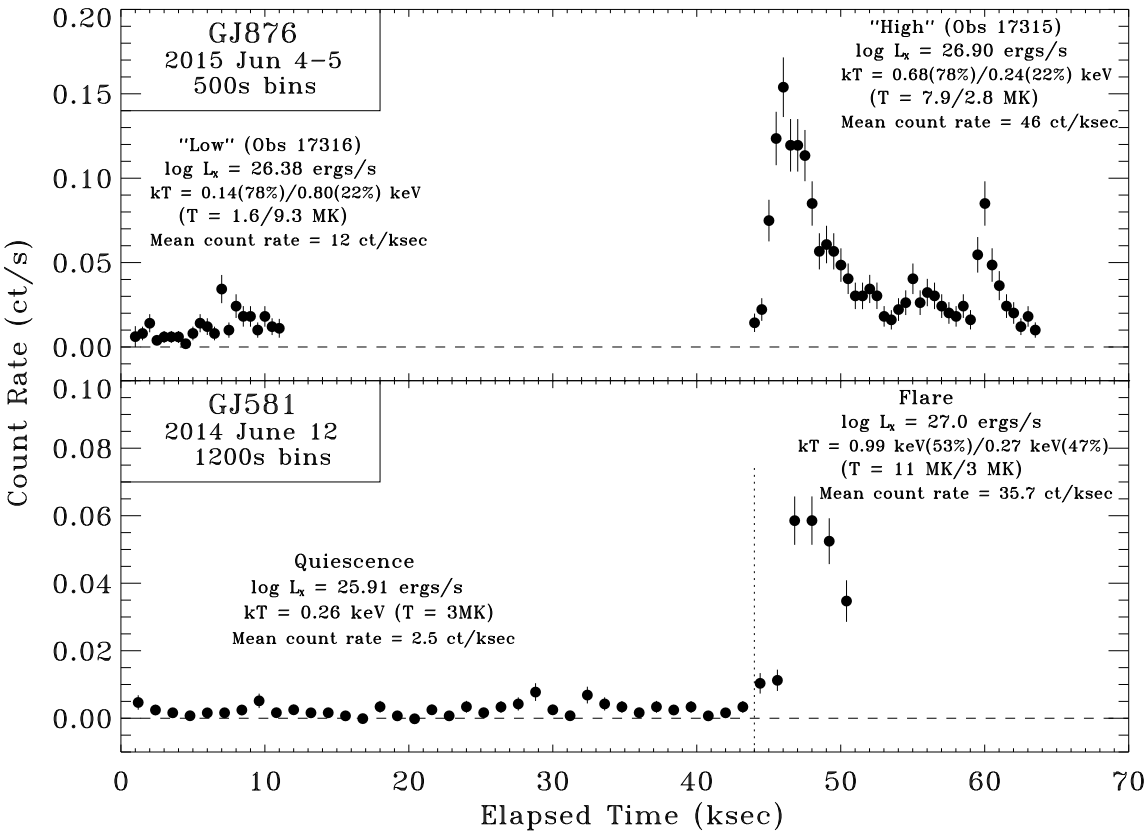

Figure 4. Chandra ACIS-S3 light-curves of GJ 876A (M4 V; P_{rot} = 81 d) and GJ 581 (M3 V; P_{rot} = 132 d). Both stars have masses between 0.30 and 0.35 $M_{\odot}$ and are thus in the fully convective mass range. Despite having long rotation periods, both stars show dramatic coronal flaring. 1σ error bars are plotted. The vertical dotted line in the GJ 581 figure marks the time split between the quiescent and flaring time intervals – the quiescent exposure totals 40.6 ksec, while the flare is observed for 7.0 ksec .

were 1.24×10^{31} ergs and 2.72×10^{30} ergs, respectively. The total integrated energy during the "High" observation was 1.54×10^{31} ergs. For direct comparison to solar flares, the soft X-ray flux in the GOES 1-8 Å (1.55-12.4 keV) passband was estimated (see Youngblood et al. (2017)). During the peak of the largest flare a 1T XSPEC coronal temperature of 0.73 keV was measured. At this time 11.2% of the Chandra flux fell in the GOES SXR band, and thus implies a "GOES" flux of $8.2^{+0.8}_{-1.0} \times 10^{-14}$ erg cm^{-2} s^{-1} and effects equivalent to a M9.5 (error range M7.8-X1.1) solar flare in the habitable zone of GJ876A. Youngblood et al. (2017) provide a detailed discussion of the potential impact of flare radiation and particle fluxes in this star's habitable zone.

GJ 581 (M3 V) : Despite showing slow rotation with period estimates of 132.5 ±6.3 days (Suárez Mascareño et al. 2015) and 130±2 days (Robertson, Mahadevan, Endl, & Roy 2014), the Chandra observation of GJ 581 showed a major flare (see Fig. 4). The flare peak was at a flux level more than 20 times quiescence. During the flare half the emission was from plasma with a characteristic temperature of 1.0 keV (11 MK), while the other half was near the quiescent temperature of 0.27 keV (3 MK) but with twice the quiescent volume emission measure. The flare is seen for 7 ks until the end of the observation, when the emission is still far above the quiescent level.

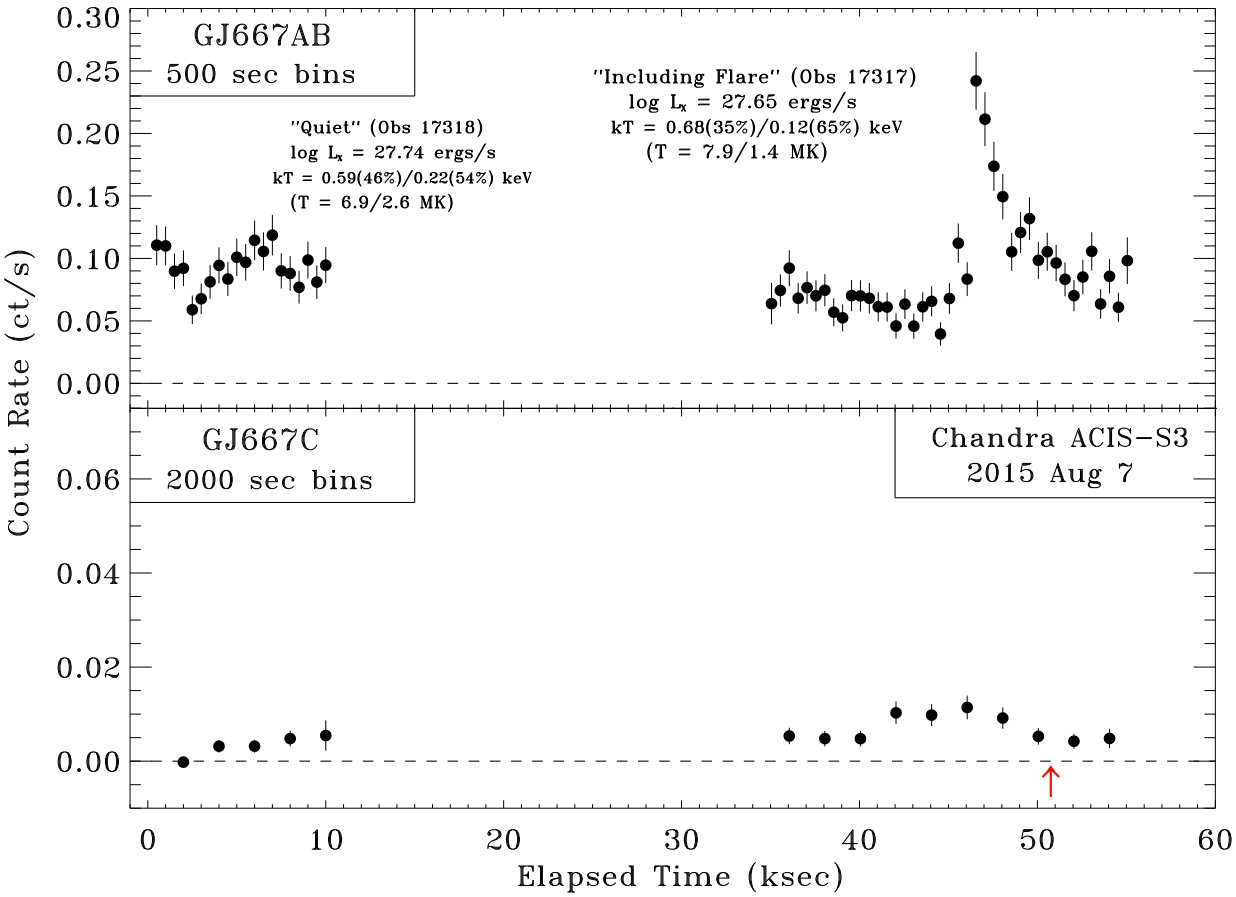

Figure 5. Chandra ACIS-S3 light curves of the K3+K5 binary GJ 667AB (upper panel) using 500 second binning and GJ 667C (lower panel) using 2 kilosecond sampling bins. 1σ error bars are plotted. Note that the GJ 667C y-axis covers only one quarter the count rate range of the GJ667AB plot. GJ 667C is only a weak source and no statistically significant variability is detected. A red upward arrow marks the time when an FUV flare was detected (Loyd et al. 2018).

GJ 667C (HD156384C, M1.5 V): This M dwarf is the tertiary component in a hierarchical triple star system with the more massive A (K3) and B (K5) components forming a 42 yr period binary (Malkov et al. 2012). Fig. 5 shows the X-ray light curves for the C and combined AB components. GJ 667C is a weak non-variable source but the AB pair shows variable X-ray emission with one obvious flare. For GJ 667C an FUV flare was seen during simultaneous HST observations (Loyd et al. 2018) but no X-ray counterpart is visible. The A and B components are barely separated by ACIS with GJ 667A being the brighter X-ray source contributing ∼70-75% of the X-ray emission of the K dwarf pair. The mean X-ray luminosity of GJ 667AB is 4.86 $\times$ 10^{27} erg s^{-1} with almost equal fluxes measured from the two Chandra observations, The X-ray to bolometric luminosity ratio for the combined AB signal is log L_X/L_{bol} ∼ -5.5.

GJ 674 (M3 V): Two XMM-Newton datasets exist for GJ 674. During our 2018 observation some weak variability was seen but the observations ended at 14:40 on 2018 Apr 3 just minutes before the onset of the giant FUV flare observed by HST (Froning et al. 2019). However, observation 0551020101 (PI Schmitt) on 2008 Sep 5 contained one large and two small X-ray flares (Poppenhaeger, Robrade, & Schmitt 2010). The EPIC pn lightcurves are shown in Fig. 6. The quiescent count rates are almost identical in the two observations. The average X-ray luminosity during the larger 2008 flare is 8.9 $\times$ 10^{27} erg s^{-1} (log L_X = 27.95 erg s^{-1}) and the peak luminosity is 1.5 $\times$ 10^{28} erg s^{-1} (log L_X = 28.17 erg s^{-1}). The duration of the flare was 5.3 ks. The integrated net flare energy (i.e. after subtraction of the quiescent emission) is 3.0 $\times$ 10^{31} ergs.

GJ 729 (Ross 154; M4 V): This star is the youngest fully-convective star in the sample with a rotation period of 2.848 days (Newton et al. 2016) and an age of less than 1 Gyr based on its membership in the Castor Moving Group (Allen & Herrera 1998). Persistent X-ray variability is seen in XMM-Newton observations (see Fig. 7), including our Mega-MUSCLES observation in 2018 and an earlier 68 ksec observation in 2010 (ObsID: 0601950101, PI Wargelin). The largest 2010 flare has average X-ray luminosity of 8.8 $\times$ 10^{27} erg s^{-1} (log L_X = 27.94 erg s^{-1}) and the peak luminosity is 1.92 $\times$ 10^{28} erg s^{-1} (log L_X = 28.28 erg s^{-1}). The integrated net flare energy (i.e. after subtraction of the quiescent emission) is 7.26 $\times$ 10^{30} ergs, which is roughly twice the quiescent emission emitted during the 1.5 ks flare duration.

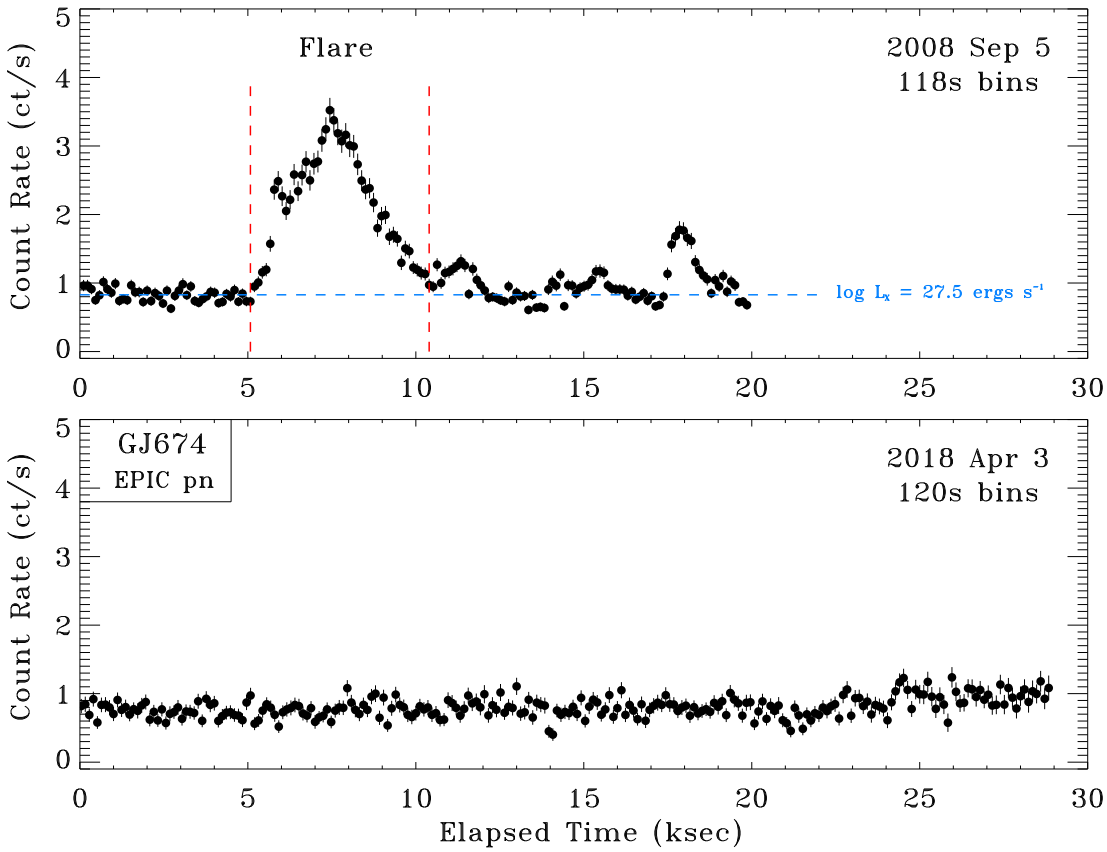

Figure 6. XMM-Newton EPIC pn light-curves of the young star GJ 674 (M3V; P_{rot} = 33 d). This star has a mass of 0.35 $M_\odot$ and thus lies right at the fully convective boundary. GJ 674 showed significant X-ray flaring in 2008 but little variability in 2018. However, immediately after the 2018 XMM-Newton observation ended an extremely large, high temperature FUV flare was seen by HST COS (Froning et al. 2019). Dashed vertical lines delineate the large 2008 flare. 1σ error bars are plotted.

GJ 729 has a history of dramatic X-ray flaring, with very large flares seen in previous Chandra ACIS and HRC observations (Wargelin et al. 2008). During the 2002 Sep 9 ACIS-S observation the X-ray luminosity rose from a quiescent level of 9 $\times$ 10^{27} erg s^{-1} to a peak of 1.8 $\times$ 10^{30} erg s^{-1}. The flare peak showed a dominant temperature component at $\sim$3 keV (35 MK).

LHS 2686 (M4.5 V) : The age of LHS 2686 is unknown but its Chandra light curve (see Fig. 8) is highly variable with at least 2 flares present and a glvary VARINDEX of 8. LHS 2686 is likely to be young (age $\leq$ 1 Gyr) based on this level of flaring, its strong Hα emission, and its high X-ray luminosity and coronal temperature.

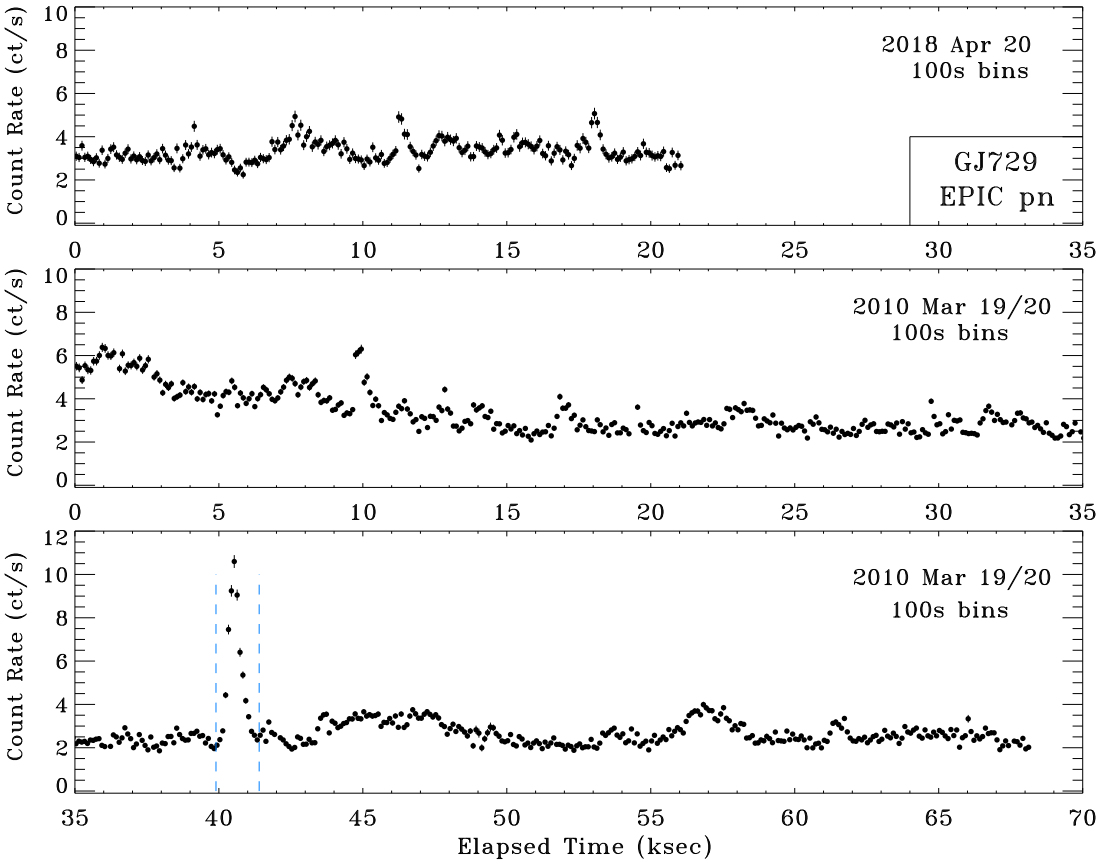

Figure 7. XMM-Newton EPIC pn light-curves of the young star GJ 729 (M4V; P_{rot} = 2.85 d) from observations in 2018 and 2010. GJ 729 shows persistent X-ray flaring. Dashed vertical lines delineate the 2010 flare discussed in the text. 1σ error bars are plotted.

GJ 699 (Barnard's Star; M4 V) : Barnard's Star is a prototypical example of an old inactive M dwarf star with a rotation period of 145 days and its proximity to the Sun allows very sensitive measurements of stellar activity. GJ 699 has the lowest quiescent X-ray luminosity (log L_X = 25.29 erg s^{-1}) of all the stars in our sample (see Table 6 and Fig. 1) and has the lowest M dwarf L_X/L_{bol} ratio. Despite this low activity level, our Chandra data contain a significant X-ray flare and COS spectra also show dramatic FUV flares (France et al. 2020). The Chandra ACIS light curve is shown in Fig. 8 and these data produce a glvary VARINDEX of 7. At the peak of the flare the X-ray flux is 2.5 $\times$ 10^{-13} erg cm^2 s^{-1} (corresponding to log L_X = 26.00 erg s^{-1}), which is just over 5 times larger than the quiescent flux. The integrated flare energy, after subtraction of the quiescent emission, is 1.6 $\times$ 10^{29} ergs and corresponds to the equivalent of a solar X2-3 flare in the habitable zone of Barnard's Star. Flares of this size occur roughly once per month on the

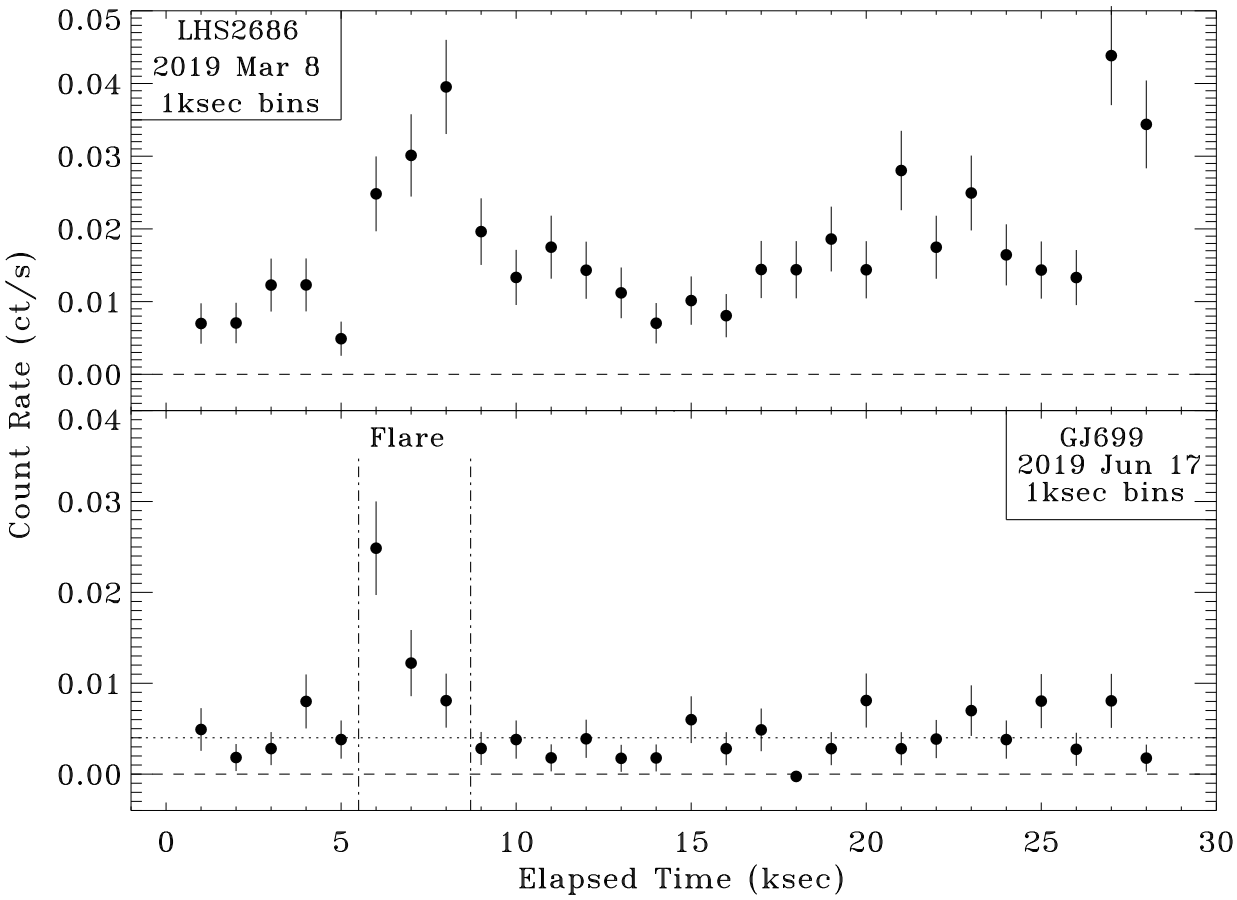

Figure 8. Chandra ACIS-S3 light curves of LHS 2686 (M4.5 V; P_{rot} = 29 d) and GJ 699 (M4 V; P_{rot} = 145 d). These stars are likely to be fully convective having masses near 0.16 $M_{\odot}$. While GJ 699 is a slow rotator and LHS2686 is a much faster rotator, both stars show significant flaring. Both plots are for 1 kilosecond sampling bins. 1σ error bars are plotted.

Sun. During a total monitoring duration of 52 ksec (0.6 days), the MegaMUSCLES non-simultaneous COS and Chandra observations detected 3 major flares. France et al. (2020) consider the potential CME particle fluxes that might be associated with these flares and, based on exoplanet atmospheric modeling, conclude that the quiescent radiation field would drive minimal atmospheric erosion but that flare conditions would produce significant erosion from any habitable zone planets.

GJ 1132 (M4 V): This weak source possibly shows a rise in the count rate towards the end of the observation, but the observation suffers from high background radiation levels.

TRAPPIST-1 (M8 V) : During the 2018 December 18 XMM-Newton observation of TRAPPIST-1 only weak X-ray emission was detected at a count rate of 0.005 ct s^{-1} , corresponding to log L_X =26.33 ergs s^{-1}. Even long XMM-Newton observations have recorded too few events to allow detailed variability studies and most observations overlap in estimated X-ray flux and luminosity. In earlier observations with the same instruments Wheatley et al. (2017) detected variable emission but, within the error bars, the source properties overlap with those from our 2018 observation.

7. RESULTS AND DISCUSSION

7.1. *Coronal Thermal Structure*

Spectral fitting of the CCD resolution X-ray spectra using XSPEC provides valuable information on the coronal thermal structure but is limited by the available X-ray signal with lower count levels providing less information. In Fig. 9, spectra for low activity and high activity Chandra observations of GJ 876 are shown

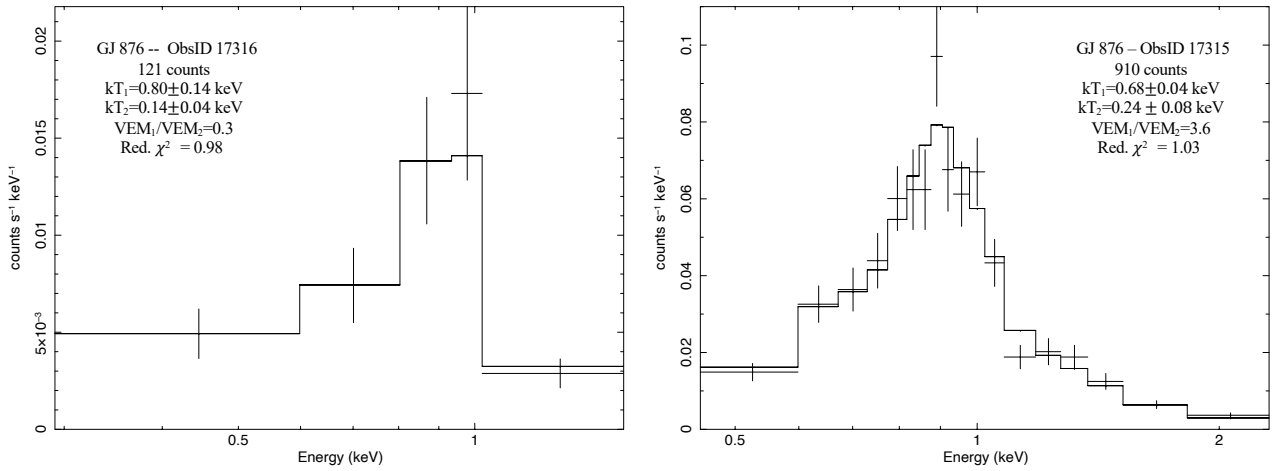

Figure 9. Examples of XSPEC spectral fitting to Chandra CCD-resolution spectra of GJ 876. These figures demonstrate the fitting framework within XSPEC. The spectral data with associated error bars are overlaid on the final model shown as a histogram. Right panel: a two-temperature (2-T) fit to the high activity (ObsID 17315) spectrum grouped with 35 events per channel. Left panel: a 2-T fit to the low activity (ObsID 17316) spectrum, recorded 12 hours earlier, grouped with 15 events per channel.

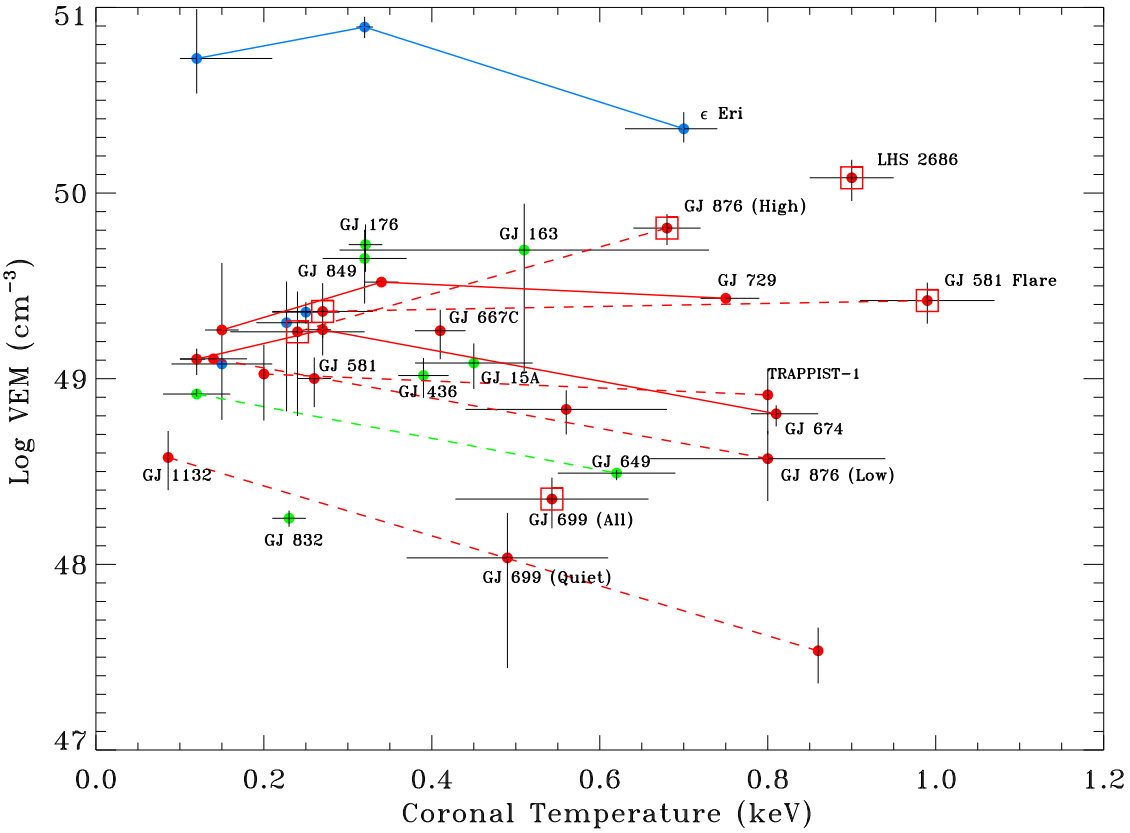

Figure 10. Volume emission measure as a function of coronal temperature. The highest volume emission measure marks the dominant coronal thermal component for each star. The coronal temperatures for GJ 1132 and TRAPPIST-1 are assumed values and not measured values from the spectral fits. Dashed lines connect the characteristic temperatures from 2 temperature fits. For clarity, the characteristic temperatures from 3 temperature fits are connected by solid lines. Square boxes mark data dominated by flare plasma. Color coding as in Fig. 1.

as examples. The amount of coronal plasma (volume emission measure – VEM) as a function of coronal temperature measured from the CCD-resolution spectra is shown in Fig. 10. The coronal temperatures show the expected behavior where quiescent plasma is at cooler temperatures than flaring plasma. The quiescent emission for all the stars shows a dominant VEM component peaking at a fairly cool temperature in the range 0.2-0.5 keV (2 - 6 MK), with many stars clustering near 0.25 keV (3 MK). Note that for GJ 1132 and TRAPPIST-1 the coronal temperatures have been assumed rather than measured. Flaring time intervals show higher characteristic temperatures in the range 0.6-1.0 keV (7 - 12 MK). It should always be remembered that "quiescent" conditions may contain low level, unrecognized flaring.

7.2. *Activity Trends of Sample*

Mass and Effective Temperature: The plots of X-ray luminosity against mass and effective temperature (Fig. 1) convey essentially the same information because the two parameters are directly connected. As expected younger, more rapidly rotating stars show higher X-ray luminosities (Pallavicini et al. 1981; Walter 1982; Pizzolato et al. 2003). At any particular mass or effective temperature there is a significant range in X-ray luminosity and some of that range can definitely be associated with variable flaring X-ray emission. X-rays provide a larger contribution to the overall bolometric luminosity for lower mass stars; a feature that becomes prominent when viewing the ratio of X-ray to bolometric luminosity.

Rotation and Age: It is well known that rapid rotation drives dynamos that create the magnetic activity resulting in X-ray and UV radiation. This correlation has been developed using ground-based optical data (Noyes et al. 1984; West et al. 2015; Houdebine et al. 2017) and explicitly for coronal emission from space-based X-ray data (Pizzolato et al. 2003; Magaudda et al. 2020; Johnstone, Bartel, & Güdel 2021). The correlation between rotation and magnetic activity extends across the divide between mid-M dwarfs with a radiative core and fully convective late-M dwarfs without any dramatic changes (Wright et al. 2018; Linsky et al. 2020). Initially, young M dwarfs are fast rotators showing saturated coronal emission with log $L_X/L_{bol} \simeq$ -3 . Stars such as GJ 729 and GJ 674 in our sample are typical examples of such very active coronae. As stars grow older their rotation usually slows and magnetic activity declines. However, age is not a controlling factor, because an old but rapidly rotating star can still be magnetically active, e.g. TRAPPIST-1, which shows a high log L_X/L_{bol} ratio despite being at least as old as the Sun, based on the kinematic and elemental abundance age estimate of Burgasser & Mamajek (2017).

Rossby Number: Fig. 11 displays log-log plots comparing the ratio of the 0.3-10.0 keV X-ray luminosity to bolometric luminosity as a function of rotation period and the X-ray luminosity to bolometric luminosity in the ROSAT 0.1-2.4 keV energy range as a function of Rossby number.

Wright et al. (2018) and Wright et al. (2011) performed detailed studies of the relationship between X-ray luminosity in the ROSAT 0.1-2.4 keV energy range and stellar rotation for a wide range of FGKM dwarf stars. They found that the tightest correlations involved the Rossby number ($R_0 = P_{rot}/\tau$, where τ is the convective turnover time), rather than the rotation period (P_{rot}) alone. The relationships discussed by

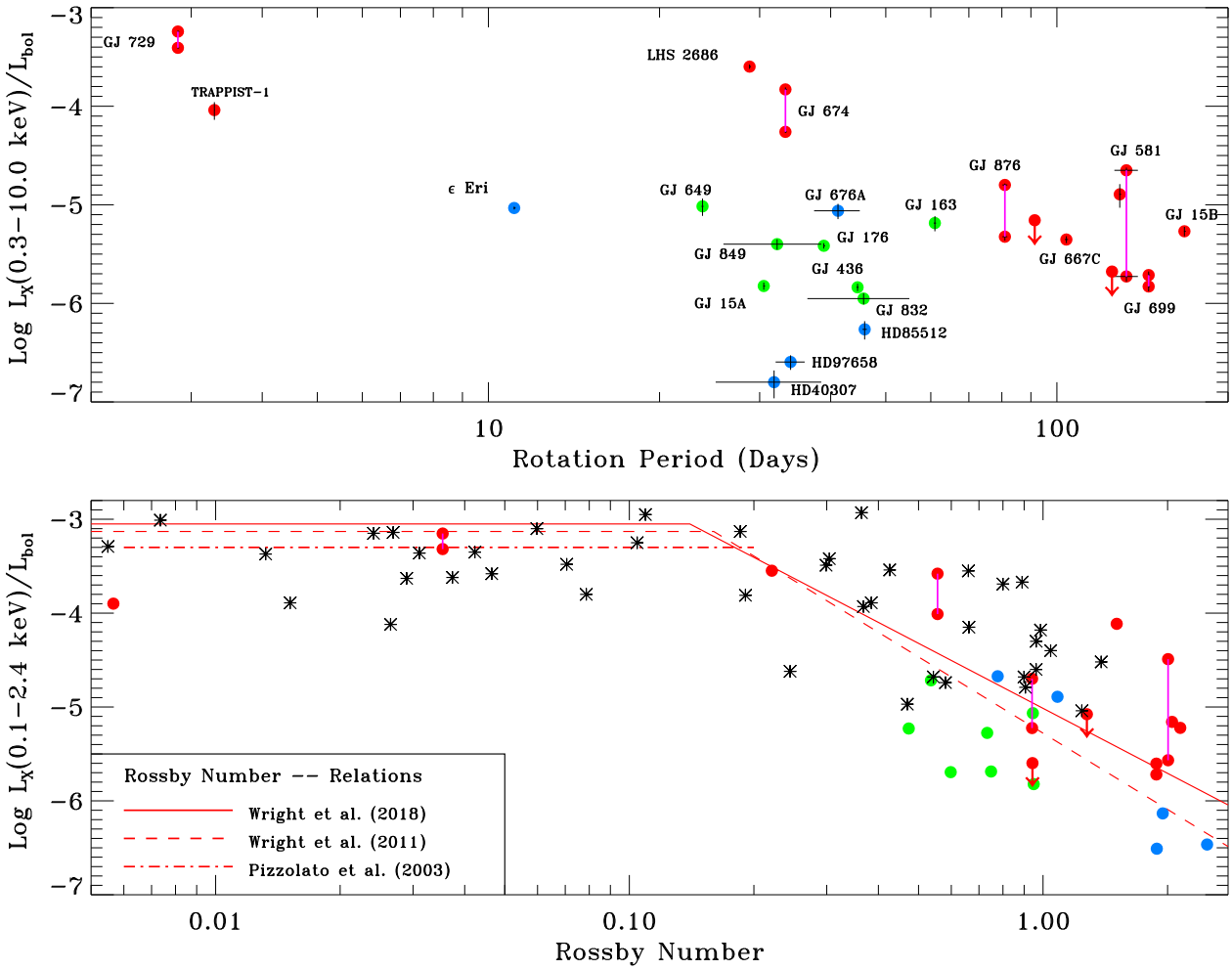

Figure 11. Comparison of X-ray-to-bolometric luminosity ratio as a function of rotational period (upper panel) and Rossby number (lower panel). The empirical relationships between the X-ray to bolometric luminosity ratio and Rossby number (rotation period/convective turnover timescale) derived by Wright et al. (2018) and Wright et al. (2011) from large samples of M dwarfs are plotted as solid and dashed lines, respectively. The saturated activity level for M dwarfs from Pizzolato et al. (2003) is shown as a dot-dash line. The nearby M dwarf sample from Wright et al. (2018) and Wright et al. (2011) are shown as black asterisks. Color coding as in Fig. 1.

Wright et al. (2018) and Wright et al. (2011) are plotted in Fig 11. Declines from saturated emission start at R_0 = 0.14 and 0.16. As a guide to the range of coronal activity detected, the sample of nearby M dwarfs included in those papers are also plotted. The Rossby numbers for all these stars were recalculated using Eqn. 5 of Wright et al. (2018). For the Rossby number plot the X-ray luminosities of our target stars were converted to the 0.1-2.4 keV ROSAT energy range for compatibility with the other data and relationships

shown. This energy conversion results in increased luminosities that are temperature dependent; at 0.5 keV the increase is 31%, at 0.3 keV it becomes 50%, and by 0.15 keV it is 94%.

The MUSCLES and Mega-MUSCLES stars are consistent with previous observations of M dwarf coronal emission but extend the sampling to lower X-ray luminosities, larger Rossby numbers, and smaller masses.

7.3. *Coronal Variability*

Perhaps the most important result from the MUSCLES and Mega-MUSCLES surveys is the discovery that strong UV/X-ray flare activity is present on M dwarfs even down to the oldest, slowly rotating and lowest mass stars sampled. Many of the stars observed, particularly the mid-M and late-M stars, show X-ray variability, often in the form of large flare outbursts and at other times as clear changes in quiescent flux between observations at different times. Several examples are described by Youngblood et al. (2017), including the multiple flares seen by Chandra from the slowly-rotating (P_{rot} = 97 days) M4 dwarf GJ876 (see Fig. 4). These flares when viewed from the habitable zone are remarkable in comparison to present day solar flares that impact the Earth.

FUV and X-ray flares were observed that reached peaks at 10-100 times the quiescent emission on timescales of 10^2-10^3 seconds. These observations were enabled by the temporal variability studies possible using the Cosmic Origins Spectrograph (COS) on HST (Green et al. 2012) and the photon counting X-ray imagers on Chandra and XMM-Newton. COS provides both flare-related flux and spectral line profile monitoring. Loyd et al. (2018) studied the FUV variability seen in the COS data for the MUSCLES sample and found that most of the nominally "inactive" stars showed significant flaring in transition region and chromospheric emission lines. While the FUV emission declines as M dwarfs age and rotate more slowly, the level of flaring emission relative to quiescent emission remains constant.

8. CONCLUSIONS

The MUSCLES and Mega-MUSCLES HST Treasury programs have completed a comprehensive survey of the high energy UV/EUV/X-ray radiation fields of a representative sample of nearby K-M dwarf stars hosting likely terrestrial exoplanets. These stars sample a broad range of mass/effective temperature, rota-

tional rates, and ages and should prove useful as activity proxies for more distant exoplanetary systems for which detailed observational studies may not be possible.

The overall conclusions concerning the coronal X-ray emission from this sample of stars are:

i) The vast majority of the stars (21 of 23) were detected in deep Chandra/XMM-Newton/Swift observations and useful upper limits measured for the other two. Accurate X-ray luminosities were measured to quantify the coronal activity.This was a result of selecting the nearest suitable exoplanet host stars in building the sample.

ii) Useful spectral information was obtained for most of the detected Chandra and XMM-Newton sources and this provides estimates of the coronal characteristic temperatures. This information is vital for the accurate modeling of the associated EUV radiation.

iii) Short-term and long-term coronal variability is common, particularly among the M dwarfs. Significant X-ray and UV flaring is seen, not only that expected from young fast-rotating stars, but also from slowly rotating stars older than the Sun.

This work was supported by *Chandra* grants GO4-15014X, GO5-16155X, and GO8-19017X, and NASA *XMM-Newton* grant NNX16AC09G to the University of Colorado. This work was supported by HST grants to Treasury programs 13650 and 15071. This research has made use of data obtained from the Chandra Data Archive, and software provided by the Chandra X-ray Center (CXC) in the CIAO application package. This research has made use of data from *XMM-Newton*, an ESA science mission with instruments and contributions directly funded by ESA member states and NASA. This research has made use of data and/or software provided by the High Energy Astrophysics Science Archive Research Center (HEASARC), which is a service of the Astrophysics Science Division at NASA/GSFC. This work has made use of data from the European Space Agency (ESA) mission *Gaia* (https://www.cosmos.esa.int/gaia), processed by the *Gaia* Data Processing and Analysis Consortium (DPAC, https://www.cosmos.esa.int/web/gaia/dpac/consortium). Funding for the DPAC has been provided by national institutions, in particular the institutions participating in the *Gaia* Multilateral Agreement.

Facilities: CXO, XMM-Newton, Swift, HST(COS)

Software: CIAO (Fruscione et al. 2006), XSPEC (Arnaud 1996), IDL (Ver. 8.8; Excelis Visual Information Solutions, Boulder, CO)

APPENDIX

A. LIGHT CURVES OF NON-VARIABLE SOURCES

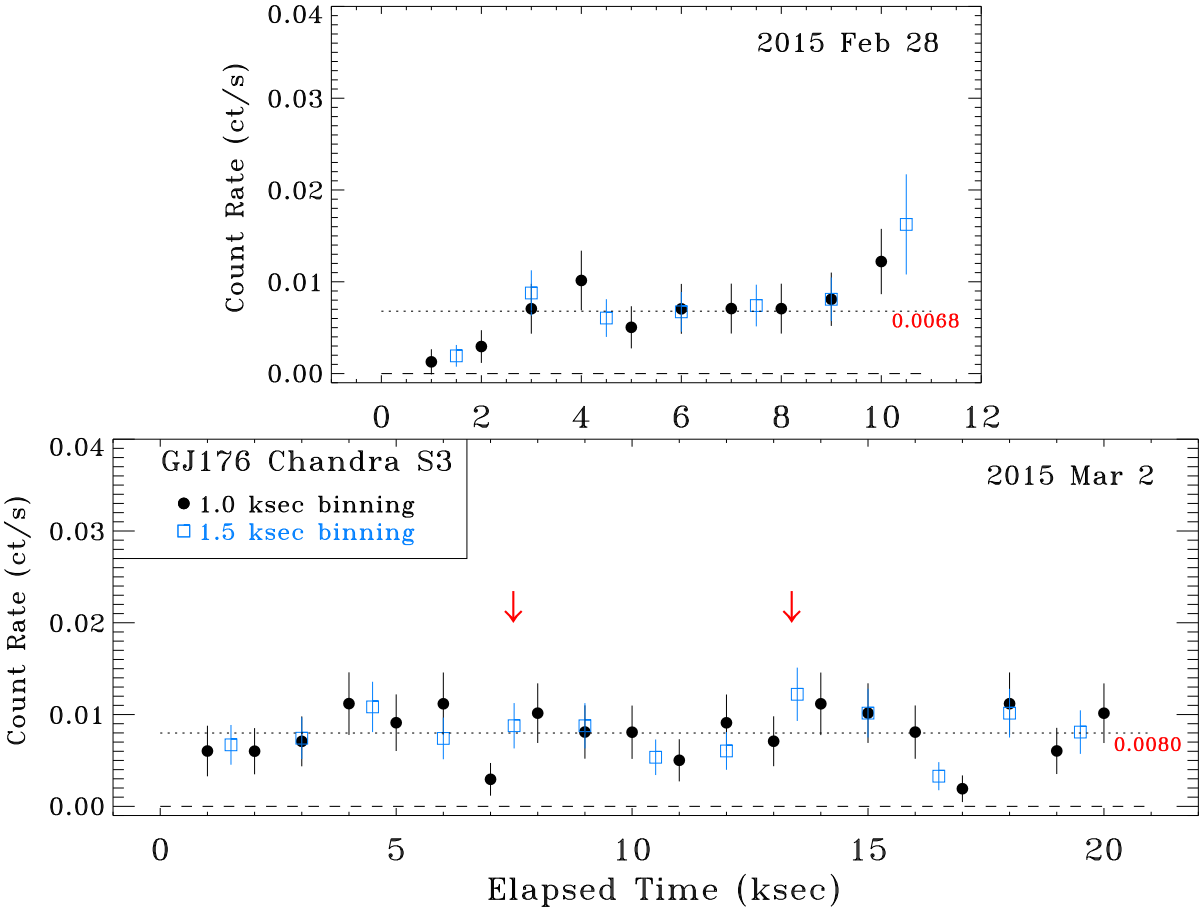

Figure 12. Chandra ACIS-S3 light curves using 1.0 and 1.5 kilosecond sampling bins from both observations of GJ 176 (M2 V). The mean count rate levels are shown as dotted lines and labeled in red. Dashed lines mark the zero count rate level. Red downward arrows marks the times when the largest FUV flares seen by Loyd et al. (2018) were detected. 1σ error bars are plotted.

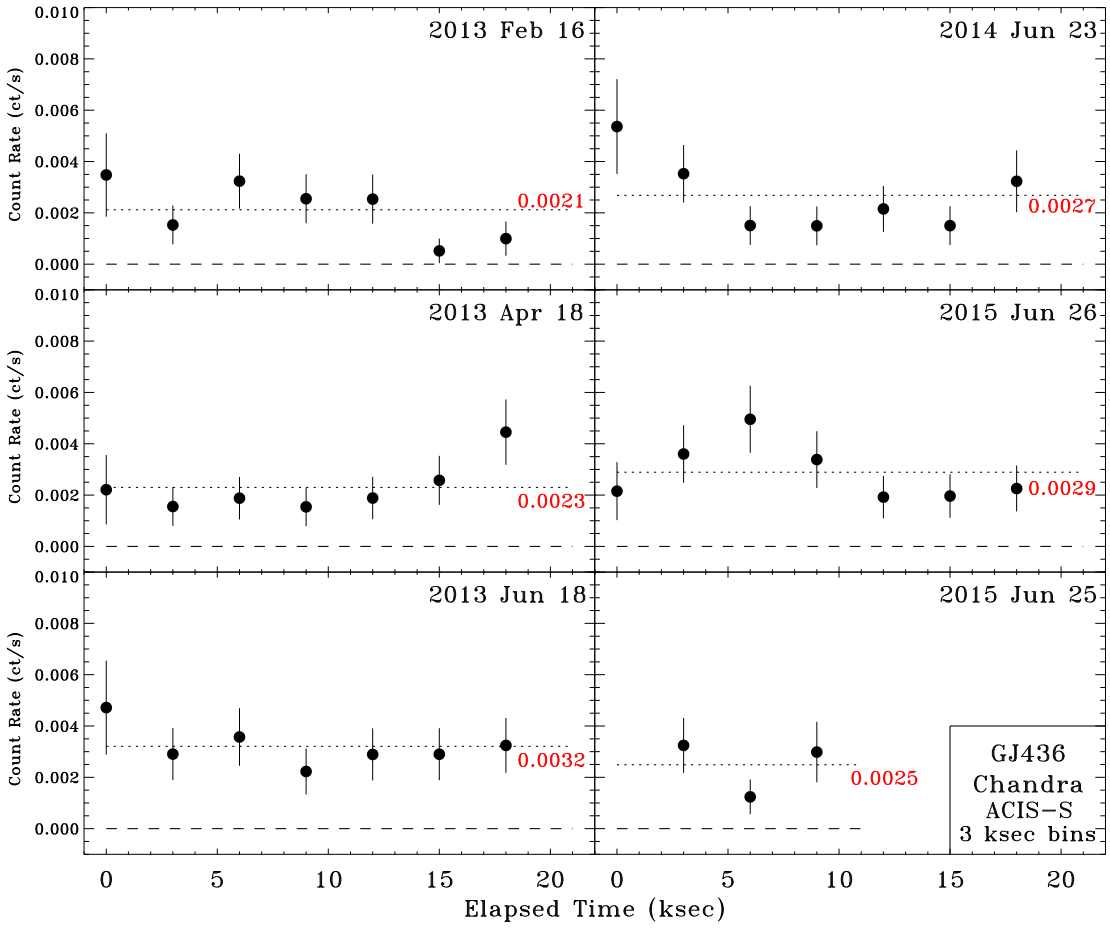

Figure 13. Chandra ACIS-S3 light curves using 3 kilosecond sampling bins from six observations of GJ 436 (M3 V). No statistical significant variability is detected over the complete dataset, which includes a total of 105 kiloseconds of X-ray monitoring.The mean count rates for the individual observations are listed in the relevant panel and marked by a dotted line. The average of the 6 measured count rates is 0.0026±0.0004 ct/s. 1σ error bars are plotted.

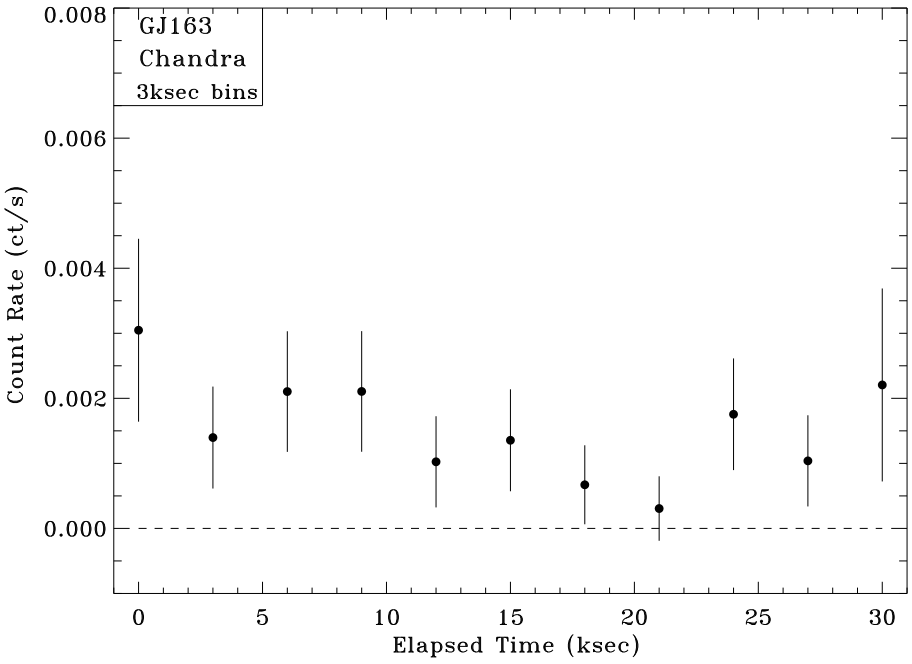

Figure 14. Chandra ACIS-S3 light curve of GJ 163 (M3.5 V, 0.405 $M_{\odot}$) using 3 kilosecond sampling bins. 1σ error bars are plotted. No statistically significant variability is detected with a glvary VARINDEX = 2.

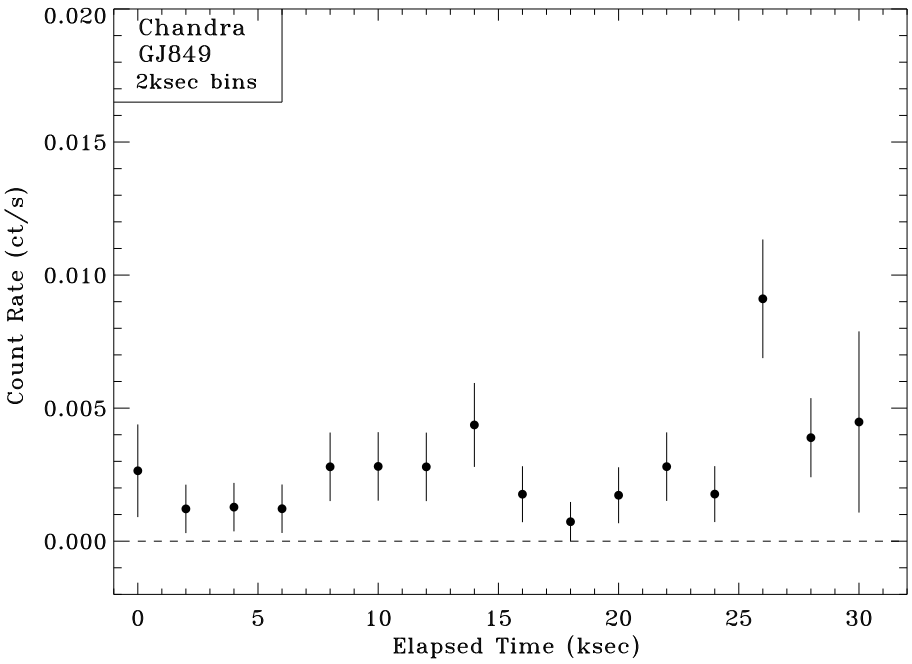

Figure 15. Chandra ACIS-S3 light curve of GJ 849 (M3.5 V, 0.465 $M_{\odot}$) using 2 kilosecond sampling bins. 1σ error bars are plotted. No statistically significant variability is detected with a glvary VARINDEX = 0.

REFERENCES

Afram, N. & Berdyugina, S.V. 2019, A&A, 629, A83

Allen, C. & Herrera, M. A. 1998, RMxAA, 34, 37

Alonso-Floriano, F. J., Morales, J. C., Caballero, J. A., et al. 2015, A&A, 577, A128

Anglada-Escudé, G., Tuomi, M., Gerlach, E., et al. 2013, A&A, 556, A126

Arnaud, K. A. 1996, *in* Astronomical Data Analysis Software and Systems V, eds. G. Jacoby and J. Barnes, ASP Conf. Series Vol. 101, p.17

Berta-Thompson, Z. K., Irwin, J., Charbonneau, D., et al 2015, Nature, 527, 2004.

Bonfanti, A., Ortolani, S., Piotto, G., & Nascimbeni, V. 2015, A&A, 575, A18

Bonfils, X., Lo Curto, G., Correia, A. C. M., et al 2013, A&A, 556, A110

Bryden, G., Beichman, C. A., Carpenter, J. M., et al. 2009, ApJ, 705, 1226

Burgasser, A. J. & Mamajek, E. E. 2017, ApJ, 845, 110

Chabrier, G. & Baraffe, I. 1997, A&A, 327, 1039

Coffaro, M., Stelzer, B., Orlando, S., et al. 2020, A&A, 636, A49

Díez Alonso, E., Caballero, J. A., Montes, D. et al. 2019, A&A, 621, A126

Donahue, R. A., Saar, S. H., & Baliunas, S. L. 1996, ApJ, 466, 384

Dorman, B., Arnaud, K. A., & Gordon, C. A. 2003, BAAS35, 641

Dressing, C. D. & Charbonneau, D., 2015, ApJ, 807, 45

Duvvuri, G. M., Pineda, J. S., Berta-Thompson, Z. K., et al. 2021, ApJ, 913, 40

Fleming, T. A., Schmitt, J. H. M. M., & Giampapa, M. S. 1995, ApJ, 450, 401

France, K., Duvvuri, G., Egan, H., et al. 2020, AJ, 160, 237

France, K., Froning, C. S., Linsky, J. L., et al. 2013, ApJ, 763, 149

France, K., Linsky, J. L., Tian, F., et al. 2012, ApJL, 750, L32

France, K., Loyd, R. O. P., Youngblood, A., et al. 2016, ApJ, 820, 89

Froning, C. S., Kowalski, A., France, K. et al. 2019, ApJL, 871, L26

Froning, C. S., Wilson, D., France, K. et al. 2022, BAAS, 54e.023F

Fruscione, A., McDowell, J. C., Allen, G. E., et al. 2006, SPIE, Vol. 6270, id. 62701V

Gaia Collaboration et al. 2016, A&A, 595,A1

Gaia Collaboration et al. 2020, arXiv:2012.01533

Gonzales, E. C., Faherty, J. K., Gagné, J. , et al. 2019, ApJ, 886, 131

Green, J.C., Froning, C.S., Osterman, S., et al. 2012, ApJ, 744, 60

Güdel, M. 2007, LRSP., 4, 3

Guo, X., Crossfield, I. J. M., Dragomir, D., et al. 2012, AJ, 159, 239

Hawley, S. L., Gizis, J. E., & reid, I. N. 1996, AJ, 112, 2799

Houdebine, E. R., Mullan, D. J., Bercu, B., et al. 2017, ApJ, 837, 56

Houdebine, E. R., Mullan, D. J., Doyle, J. G. et al. 2019, AJ, 158, 96

Ibañez Bustos, R. V., Buccino, A. P., Messina, S., Lanza, A. F., & Mauas, P. J. D. 2020, A&A, 644, A2

Janson, M., Reffert, S., Brandner, W., et al., 2008, A&A, 488, 771

Johnstone, C. P., Bartel, M., & Gúdel, M. 2021, A&A, 649, A96

Kiraga, M. & Stepień, K. 2007, AcA, 57, 149

Koen, C., Kilkenny, D., van Wyk, F., & Marang, F. 2010, MNRAS, 403,1949

Kulenthirarajah, L., Donati, J.-F., Hussain, G., Morin, J., & Allard, F. 2017, MNRAS, 487, 1335

Linsky, J. L., Wood, B. E., Youngblood, A., et al. 2020, ApJ, 902,3

Loyd, R. O. P., France, K., Youngblood, A., et al. 2016, ApJ, 824, 102

Loyd, R. O. P., France, K., Youngblood, A., et al. 2018, ApJ, 867, 71

Magaudda, E., Stelzer, B., Covey, K. R., et al. 2020, A&A, 638, A20

Malkov, O. Yu., Tamazian, V. S., Docobo, J. A., & Chulkov, D. A. 2012, A&A, 546, 69

Mallonn, M., Herrero, E., Juvan, I. G., et al. 2018, A&A, 614, A35

Mann, A. W., Dupuy, T., Kraus, A. L., et al. 2019, ApJ, 871, 63

Metcalfe, T. S., Buccino, A. P., Brown, B. P., et al. 2013, ApJL, 763, L26

Montes, D., López-Santiago, J., Gálvez, M. C., et al. 2001, MNRAS, 328, 45

Newton, E. R., Charbonneau, D., Irwion, J., et al., 2014, AJ, 147, 20

Newton, E. R., Irwin, J., Charbonneau, D., et al., 2016, ApJ, 821, 93

Newton, E. R., Mondrik, N., Irwin, J., Winters, J. G., & Charbonneau, D. 2018, AJ, 156, 217

Noyes, R. W., Hartmann, L. W., Baliunas, S. L., Duncan, D. K., & Vaughan, A. H. 1984, ApJ, 279, 763

Pallavicini, R., Golub, L., Rosner, R., et al. 1981, ApJ, 248, 279

Pinamonti, M., Damasso, M., Marzari, F., et al. 2018, A&A, 617, A104

Pineda, J. S., Youngblood, A. & France, K. 2021b, ApJ, 918, 40

Pizzolato, N., Maggio, A., Micela, G., Sciortino, S., & Ventura, P. 2003, A&A, 397, 147

Poppenhaeger, K., Robrade, J., & Schmitt, J. H. M. M. 2010, A&A, 515, A98

Reid, I. N., Hawley, S. L., & Gizis, J. E. 1995, AJ, 110, 1838

Ribas, I., Guinan, E. F., Güdel, M., & Audard, M. 2005, ApJ, 622, 680

Ribas, I., Tuomi, M., Reiners, A. et al. 2018, Nature, 563, 365

Rivera, E. J., Lissauer, J. J., Butler, R. P., et al. 2005, ApJ, 634, 625

Robertson, P., Mahadevan, S., Endl, M., & Roy, A. 2014, Science, 345, 440

Schweitzer, A., Passegger, V. M., Cifuentes, C. et al. 2019, A&A, 625, A68

Shulyak, D., Reiners, A., Nagel, E., et al. 2019, A&A, 626, A86

Smith, R. K., Brickhouse, N. S., Liedahl, D. A., & Raymond, J. C. 2001, ApJL, 556, L91

Sousa, S. G., Santos, N. C., Mayor, M., et al. 2008, A&A, 487, 373

Suárez Mascareño, A., Rebolo, R., González Hernández, J. I., Esposito, M. 2015, MNRAS, 452, 2745

Takeda , Y. & Honda, S. 2020, AJ, 159, 174

Toledo-Padrón, B., González hernández, J. I., Rodríguez-López, et al. 2019, MNRAS, 488, 5145

Tuomi, M., Anglada-Escudé, G., Gerlach, E., et al. 2013, A&A, 549, A48

Van Grootel, V., Gillon, M., Valencia, D., et al. 2014, ApJ, 786, 2

Veyette, M. J. & Muirhead, P. S. 2019, ApJ, 863, 166

Vida, K., Kövári, Zs., Pál, A., Oláh, & Kriskovics, L. 2017, ApJ, 841, 124

Walter, F. M. 1982, ApJ, 253, 745

Wargelin, B. J., Kashyap, V. L., Drake, J. J., García-Alvarez, D., & Ratzlaff, P. W. 2008, ApJ, 676, 610

West, A. A., Weisenburger, K. L., Irwin, J., at al. 2015, ApJ, 812, 3

Wheatley, P. J., Louden, T., Bourrier, V., Ehrenreich, D., & Gillon, M. 2017, /mnras, 465, L74

Wilson, D. & The Mega-MUSCLES Collaboration 2021, https://doi.org/10.5281/zenodo.4567579

Wright, N. J., Drake, J. J., Mamajek, E. E., & Henry, G. W. 2011, ApJ, 743, 48

Wright, N. J., Newton, E. R., Williams, P. K. G. Drake, J. J., & Yadav, R. K. 2018, MNRAS, 479, 2351

Youngblood, A., France, K., Loyd, R.O.P., et al. 2017, ApJ, 843, 31

Youngblood, A., France, K., Loyd, R.O.P., et al. 2016, ApJ, 824, 101